ISSN 1949-8470 (online)

World Journal of *Radiology*

World J Radiol 2023 January 28; 15(1): 1-31

Published by Baishideng Publishing Group Inc

World Journal of Radiology

Contents

Monthly Volume 15 Number 1 January 28, 2023

MINIREVIEWS

ORIGINAL ARTICLE

Retrospective Study

World Journal of Radiology

Monthly Volume 15 Number 1 January 28, 2023

Contents

ABOUT COVER

Editorial Board Member of *World Journal of Radiology*, Fernando Santiago, PhD, Doctor, Professor, Teacher, Department of Radiology, Santiago, FR (reprint author), Hosp Traumatol Ciudad Sanitaria Virgen de las Nie, Dept Radiol, Carretera Jaen SN, Granada 18013, Spain. ferusan12@gmail.com

AIMS AND SCOPE

The primary aim of *World Journal of Radiology* (*WJR*, *World J Radiol*) is to provide scholars and readers from various fields of radiology with a platform to publish high-quality basic and clinical research articles and communicate their research findings online.

WJR mainly publishes articles reporting research results and findings obtained in the field of radiology and covering a wide range of topics including state of the art information on cardiopulmonary imaging, gastrointestinal imaging, genitourinary imaging, musculoskeletal imaging, neuroradiology/head and neck imaging, nuclear medicine and molecular imaging, pediatric imaging, vascular and interventional radiology, and women's imaging.

INDEXING/ABSTRACTING

The *WJR* is now abstracted and indexed in PubMed, PubMed Central, Emerging Sources Citation Index (Web of Science), Reference Citation Analysis, China National Knowledge Infrastructure, China Science and Technology Journal Database, and Superstar Journals Database. The 2022 edition of Journal Citation Reports ® cites the 2021 Journal Citation Indicator (JCI) for *WJR* as 0.48.

RESPONSIBLE EDITORS FOR THIS ISSUE

NAME OF JOURNAL
World Journal of Radiology

ISSN
ISSN 1949-8470 (online)

LAUNCH DATE
January 31, 2009

FREQUENCY
Monthly

EDITORS-IN-CHIEF
Thomas J Vogl

EDITORIAL BOARD MEMBERS
https://www.wjgnet.com/1949-8470/editorialboard.htm

PUBLICATION DATE
January 28, 2023

INSTRUCTIONS TO AUTHORS
https://www.wjgnet.com/bpg/gerinfo/204

GUIDELINES FOR ETHICS DOCUMENTS
https://www.wjgnet.com/bpg/GerInfo/287

GUIDELINES FOR NON-NATIVE SPEAKERS OF ENGLISH
https://www.wjgnet.com/bpg/gerinfo/240

PUBLICATION ETHICS
https://www.wjgnet.com/bpg/GerInfo/288

PUBLICATION MISCONDUCT
https://www.wjgnet.com/bpg/gerinfo/208

ARTICLE PROCESSING CHARGE
https://www.wjgnet.com/bpg/gerinfo/242

STEPS FOR SUBMITTING MANUSCRIPTS
https://www.wjgnet.com/bpg/GerInfo/239

ONLINE SUBMISSION
https://www.f6publishing.com

World Journal of Radiology

Submit a Manuscript: https://www.f6publishing.com

World J Radiol 2023 January 28; 15(1): 1-9

DOI: 10.4329/wjr.v15.i1.1

ISSN 1949-8470 (online)

MINIREVIEWS

Clinical anatomy of hepatic vessels by computed tomography angiography: A minireview

Aysegul Firat, Tugce Taskindere Abbasoglu, Musturay Karcaaltincaba, Yasemin H Balaban

Specialty type: Anatomy and morphology

Provenance and peer review: Invited article; Externally peer reviewed.

Peer-review model: Single blind

Peer-review report's scientific quality classification
Grade A (Excellent): 0
Grade B (Very good): 0
Grade C (Good): C, C
Grade D (Fair): D
Grade E (Poor): 0

P-Reviewer: Rasti S, Iran; Wu SZ, China

Received: September 19, 2022
Peer-review started: September 19, 2022
First decision: October 19, 2022
Revised: November 2, 2022
Accepted: December 27, 2022
Article in press: December 27, 2022
Published online: January 28, 2023

Aysegul Firat, Tugce Taskindere Abbasoglu, Department of Anatomy, Hacettepe University Faculty of Medicine, Ankara 06100, Turkey

Musturay Karcaaltincaba, Department of Radiology, Hacettepe University Faculty of Medicine, Ankara 06100, Turkey

Yasemin H Balaban, Department of Gastroenterology, Hacettepe University Faculty of Medicine, Ankara 06100, Turkey

Corresponding author: Yasemin H Balaban, MD, Professor, Department of Gastroenterology, Hacettepe University Faculty of Medicine, Gevher Nesibe caddesi, Ankara 06100, Turkey. ybalaban@hacettepe.edu.tr

Abstract

The liver has a complex vascular anatomy with a unique dual blood supply. Clinical conditions of the liver vary widely and include disorders originating in the vascular and biliary systems as well as the parenchyma. In most vascular disorders, the effects on the liver are generally subclinical because of its abundant blood supply. However, early diagnosis of such vascular diseases can significantly reduce patient morbidity and mortality. Because imaging findings of vascular disease are not always readily apparent, diagnosis can be difficult. Computed tomography angiography is an excellent imaging modality for visualizing the vascular anatomy of patients for treatment planning. In this review article, we focus on the vascular anatomy of the liver and the imaging findings in some acute hepatic vascular diseases.

Key Words: Computed tomography angiography; Hepatic artery; Portal vein; Sinusoid; Portal triad; Periportal region

Core Tip: The liver has a complex vascular anatomy. Imaging findings may not be readily apparent in vascular disorders of the liver. Computed tomography angiography is an excellent imaging modality for visualizing the vascular anatomy of patients for treatment planning. This review article focuses on the vascular anatomy of the liver and imaging findings in some acute hepatic vascular diseases.

Citation: Firat A, Abbasoglu TT, Karcaaltincaba M, Balaban YH. Clinical anatomy of hepatic vessels by computed tomography angiography: A minireview. *World J Radiol* 2023; 15(1): 1-9
URL: https://www.wjgnet.com/1949-8470/full/v15/i1/1.htm
DOI: https://dx.doi.org/10.4329/wjr.v15.i1.1

INTRODUCTION

The liver performs a variety of metabolic processes for homeostasis, nutrition, and immune defence. For example, it is important for the removal and breakdown of toxic or potentially toxic substances from the blood; the regulation of blood glucose and lipids; the storage of certain vitamins, iron, and other micronutrients; the synthesis of proteins and clotting factors; the metabolism of amino acids; and the production of bile. It is involved in a variety of other biochemical reactions. Since most of these processes are exothermic, a significant portion of the body's thermal energy production, especially at rest, is provided by the liver. Acute clinical conditions of the liver vary widely and include disorders originating in the vascular and biliary systems as well as the parenchyma. The liver has a complex vascular anatomy with a unique dual blood perfusion. The portal vein provides 70% of the hepatic blood flow, while the hepatic artery provides the remaining 30%[1]. In most vascular disorders, the effects on the liver are generally subclinical due to this rich blood supply. However, some acute diseases of these vessels may be accompanied by abdominal pain. Early diagnosis of such vascular disease can significantly reduce patient morbidity and mortality. Computed tomography angiography (CTA) is now the standard procedure for surgical planning of living liver donors in whom most of the right lobe of liver with associated vessels and ducts, is removed for transplantation to the recipient. CTA visualises both the vascular and parenchymal anatomy of the liver. In this technique, the contrast agent is administered directly into the splanchnic bed by injection into the superior mesenteric artery. CT images acquired after an appropriate delay provide hepatic and portal phase images of the liver. Rapid image acquisition of vessels with thin sections is a critical feature of an optimal CTA protocol that prevents artefacts due to motion and respiration. Two-phase liver protocols include both an arterial and portal venous phase. CTA is an excellent imaging modality for visualising the patient's vascular anatomy for surgical planning of liver transplantation. Because imaging findings of vascular disorders may not be readily recognized, diagnosis can be difficult. In this review article, we focus on the vascular anatomy of the liver and the imaging findings in common acute diseases of the hepatic vasculature[2].

EMBRYOLOGY OF THE LIVER

The liver begins to develop from the anterior bulge of the endoderm of the foregut. From the cephalic part of this diverticular structure, splanchnic mesodermal cells migrate into the septum transversum. These cells, which concentrate around the vitelline veins, differentiate into hepatic cells as single-layered plaques. Kupffer cells also differentiate from the endothelial cells of the vitelline plexus. Biliary capillaries and cholangioles also develop from the mesenchyme between the hepatocellular plates. The vitelline veins form a plexus in the liver, which then unites with the umbilical veins and opens into the sinus venosus of the heart. Later, some portions of the vitelline veins undergo atresia and become the portal vein, which unites with the splenic vein and the superior mesenteric veins. The proximal portions of the vitelline vein join the right and left hepatic veins (RHV and LHV, respectively) between the sinus venosus and the hepatic plexus. The entire right umbilical vein and the proximal portion of the left umbilical vein, which is connected to the hepatic sinusoids, atrophy. Over time, venous blood from the placenta flows into the right vitelline vein in the liver and then directly to the heart *via* the ductus venosus, a large venous trunk that separates from the hepatic sinusoids. Meanwhile, half of the blood from the umbilical vein flows through the liver and the other half through the ductus venosus. The umbilical vein settles in the falciform ligament as the ligamentum teres, and as the liver continues to grow in the abdomen, it maintains contact with the septum transversum under the diaphragm[3].

HEPATIC ORGANIZATION

The liver has a spongy structure consisting of irregular single-row cell strands and spaces called lacunae between them. The diameter of the lacunae is larger than that of the hepatocytes. The capillaries within these lacunae are called sinusoids, which are lined with a basement membrane and are permeable to macromolecules. Kupffer cells, which are part of the reticuloendothelial system, are located around the endothelium of the sinusoids. The hexagonal cells of the cell strands are called hepatocytes. They form the critical cell layer between the sinusoids and the bile canaliculi. They have a unique polarity, with the basement membrane facing the sinusoidal endothelium, while one or more apical poles may contribute

to multiple bile canaliculi[2]. Between the endothelium of the sinusoids and the hepatocytes is a potential gap called the space of Disse. The fluid accumulated in this space is drained by the lymphatic vessels and blood capillaries. Since hepatocytes are polygonal in shape and have many facets, two or three facets are in contact with the space of Disse, while the remaining facets are in contact with the neighbouring liver cells. Bile canaliculi run between adjacent hepatocytes. Hepatocyte polarity is essential in explaining many functions of the liver. Hepatocyte strands and sinusoids run past each other in a branched and interlocking fashion, which increases metabolic exchange between the blood and biliary systems. The combination of the bile duct, hepatic artery, and hepatic portal vein is termed a portal triad. As they enter the liver, each divides into segmental branches surrounded by a perivascular fibrous capsule. The hepatic lobule is a hexagonal unit consisting of a concentric arrangement of a central vein in the middle and surrounding portal triads located at the vertices of each hexagon and hepatocyte strands, although the boundaries are not very sharp. Each portal triad is surrounded by a hepatocyte plate, which is traversed by the bile canaliculi and blood vessels. Between the portal triad and the hepatocyte strand is a gap called the space of Mall (periportal area). The hepatic lobule is perfused by the branches of the hepatic artery and portal vein at the periphery and drained by the central vein in the middle of the lobule. Blood flows centrifugally from the portal triad. Bile produced by the hepatocytes also flows centrifugally to the periphery. There is blood flow from the portal vein and hepatic artery to the hepatic vein depending on the blood pressure gradient. Each central vein opens through a sublobular vein, which eventually forms the right and LHVs, and opens into the inferior vena cava. Since there is no such blood pressure gradient in the embryo, the lobular cell arrangement is not observed, and this arrangement develops after birth. In this case, the lobule structure may change with blood pressure and blood flow[3].

Another functional concept is the liver acinus: A diamond-shaped area supplied by the terminal branches of the hepatic artery and portal vein. This small unit is important in describing functional and pathologic changes in many clinical conditions. Its short axis runs along the borders of the hepatic lobules and its imaginary long axis is located between the two central veins. The hepatocytes are located in three elliptical zones around the short axis[3-5]. The areas near the center of the acini receive more oxygenated blood because they are near the afferent vessels and are referred to as zone 1 (periportal zone). Zone 2 (intermediate zone) is the intermediate region that is more peripheral to the acini, and zone 3 is the region closest to the central vein at the end of the acini. Zone 3 is most affected by ischemic damage. The lobule and acinus formation systems, which complement each other, can be related to the gross anatomy that integrates functional modulation[6,7].

In the right and left lobes of the liver, arteries, portal veins, and bile ducts run parallel to each other. These vessels and ducts branch to disperse into segments and show many individual variations, and no anastomosis was observed between the intraparenchymal branches.

The bile duct, hepatic artery, portal vein, lymphatics, and nerves open horizontally into the porta hepatis, which is located in the middle part of the visceral surface of the liver.

CT protocol

CT examinations were performed with a 16-MDCT scanner (Somatom Sensation 16, Siemens, Germany). All patients received 100 mL of iodinated contrast material (Ultravist 300/100 mg/mL; Bayer Schering Pharma, Berlin, Germany) at a flow rate of 4 mL/s using a power injector. CT images were obtained 70 s after the injection of contrast for the portal venous phase, 15-20 s for the early arterial phase, and 30-40 s for the late arterial phase. Technical parameters were detector collimation, 1.5 mm; pitch, 1.5; gantry rotation time: 0.5 s. Axial images were reconstructed at a thickness of 2 mm and 5 mm and transferred to Picture Archiving and Communication System.

Portal vein

The portal vein is formed by the union of the superior mesenteric and splenic veins. It begins at the level of the second lumbar vertebra, where it lies behind the neck of the pancreas. It has an average length of 6.50 cm and a diameter of 1.09 cm and rises behind the first part of the duodenum. After entering the right margin of the lesser omentum anterior to the epiploic foramen, it reaches the right end of the porta hepatis and divides into right and left hepatic branches that accompany the corresponding branches of the hepatic artery, lymphatic vessels, and hepatic nerve plexus. It is located behind the common bile duct and hepatic artery in the lesser omentum. The superior gastroduodenal vein empties into the portal vein from the lower right, into the left gastric vein from the lower right, and into the right gastric vein from the right. The cholecystic vein drains into the right hepatic branch of the portal vein. The left portal vein receives only the obliterated umbilical vein. The right branch supplies segments V, VI, VII, and VIII. Segments I, II, III, and IV receives the left obliterated umbilical vein *via* the ligamentum teres. It eventually opens into intraparenchymal venules that arise at right angles from a distributive vein and are less than 0.3 mm in diameter. Blood in the branches of the portal vein and hepatic artery flows into the sinusoidal microcirculation. Blood within the sinusoids flows through the radially arranged plates and empties into the central vein[3,6,7].

Some anatomic variations in the portal venous system lead to contraindications for certain surgeries such as transplantation or increase the risk of postoperative complications. Shunt operations for portal hypertension have increased interest in portal vein anatomy and studies have shown that the portal

vein has fewer variations than the hepatic artery. Portal venous variants are frequent and account approximately 20%-35% of the population[8]: (1) The most common variant is the so-called ''portal vein trifurcation'' in which the main portal vein divides into three branches: The left portal vein, the right anterior portal vein, and the right posterior portal vein; (2) the second most common variant is a right posterior portal vein arising as the first branch of the portal vein; (3) in 10% of cases, no vein opens into the main trunk of the portal vein; (4) the left gastric vein joins the main trunk of the portal vein to the left side of the junction of the superior mesenteric vein and the splenic vein; (5) in 24% of cases, the left gastric vein joins the splenic vein; (6) the inferior mesenteric vein may drain from the junction of the splenic vein and the superior mesenteric vein into the portal vein; and (7) the inferior mesenteric vein may join with the superior mesenteric vein.

Imaging findings of disorders of the portal vein

The anatomy of the portal vein is best visualised in the coronal plane of CT angiography. Acute portal vein thrombosis is sudden blood clot formation in the portal vein lumen[9]. It can occur in cirrhosis, pylephlebitis, hematologic disorders, pancreatitis, diverticulitis of the colon, appendicitis, malignancies, and surgical procedures[10]. CT is commonly used for diagnosis and usually shows the absence/presence of enhancement within the thrombus, which is critical for characterising the thrombus (Figure 1A). Acute thrombosis is usually hyperdense on pre-contrast CT images, whereas chronic thrombosis can lead to calcifications in the portal vein and abnormal liver perfusion areas can be detected in the liver parenchyma, especially in the arterial phase[11,12]. A decrease in portal vein flow may be caused by portal vein or hepatic vein thrombosis, compression by focal masses such as abscesses, long-standing biliary obstruction, or parenchymal trauma. Pylephlebitis is defined as infectious thrombosis of either the portal vein or its intrahepatic branches or both and may lead to abscess formation in the parenchyma[13]. Diverticulitis of the colon is the most common cause of septic thrombophlebitis of the mesenteric and portal venous systems[14]. The standard treatment for acute portal vein thrombosis is anticoagulation. Portal vein aneurysms are rare and account for 3% of all venous aneuryms[15]. Most of these aneurysms are acquired, as a significant number of portal vein aneurysms are discovered in patients with underlying hepatocellular disease and portal hypertension.

Hepatic artery

The proper hepatic artery supplies the liver. It is a branch of the common hepatic artery separated from the coeliac trunk. The coeliac trunk is an anterior branch of the abdominal aorta and passes through the hiatus aorticus. It runs anteriorly and transversely over the pancreas and after a short course divides into the left gastric, splenic, and common hepatic branches. The common hepatic artery runs anteriorly and enters the lesser omentum from the right margin. Here it is located to the left of the common bile duct and anterior to the portal vein. On its way up, it branches into the gastroduodenal artery, the supraduodenal artery, and the right gastric artery. Simultaneously, it continues to ascend as the proper hepatic artery. When it reaches the porta hepatis of the liver, it branches into the right (RHA) and left (LHA) hepatic arteries. Normally, the RHA passes behind the common hepatic duct and branches into the cholecystic artery. In the portal triad, the branches of the hepatic artery run parallel to the portal vein. The arterioles distribute in the lobular parenchyma and they form a peribiliary plexus around the biliary capillaries.

The Michels' classification of the hepatic arterial anatomy with the approximate frequency of occurrence of each type of variant in the general population is shown in Table 1[16].

Classical branching of the hepatic artery is observed in around 76% of people[17]. Thus, a significant proportion of patients have a variant arterial anatomy (Figure 1B and C). Hepatic artery variations do not cause absolute contraindications for transplantation. However, being informed about these variations prior to the transplantation is a factor that would simplify the surgery, decrease the rate of contraindications, and improve the chance of technical success[16,17]: (1) The common hepatic artery, as a branch of the superior mesenteric artery, passes through or behind the pancreas and courses upward; (2) the common hepatic artery branches more proximal to the right and left hepatic artery before reaching the porta hepatis; (3) the right hepatic artery arises from the superior mesenteric artery, and the left hepatic artery arises from the coeliac trunk; (4) presence of accessory right hepatic artery originating from the superior mesenteric artery; (5) presence of accessory left hepatic artery originating from the left gastric artery; (6) presence of accessory left gastric artery coming out of the right gastric artery; and (7) the right hepatic artery crosses the common bile duct anteriorly.

These variations are also important in terms of collaterals that may occur after the ligation or occlusion of an artery. In transplantation, the mapping and perfect knowledge of hepatic vascularisation is essential for the surgeon.

Imaging findings of disorders of the hepatic artery

The vascular anatomy of the liver influences surgical interventions to minimize surgical morbidity. It is possible to diagnose hepatic arterial disorders (thrombosis, aneurysm, and dissection and pseudoaneurysm formation) preoperatively and after liver transplantation by CTA. Coronal oblique slices are ideal for evaluating hepatic arterial anatomy. If the portal venous supply of the liver is intact, occlusion

Table 1 Michels' classification of the hepatic arterial anatomy[16]

Type	Frequency (%)	Description
I	55.0	RHA, MHA, and LHA arise from common hepatic artery
II	10.0	RHA, MHA, and LHA arise from common hepatic artery; replaced LHA arises from left gastric artery
IV	1.0	Replaced RHA and LHA
V	8.0	RHA, MHA, and LHA arise from common hepatic artery; accessory LHA arises from left gastric artery
VI	7.0	RHA, MHA, and LHA arise from common hepatic artery; accessory RHA
VII	1.0	Accessory RHA and LHA
VIII	4.0	Replaced RHA and accessory LHA or replaced LHA and accessory RHA
IX	4.5	Entire hepatic trunk arises from superior mesenteric artery
X	0.5	Entire hepatic trunk arises from left gastric artery

RHA: Right hepatic artery; MHA: Middle hepatic artery; LHA: Left hepatic artery.

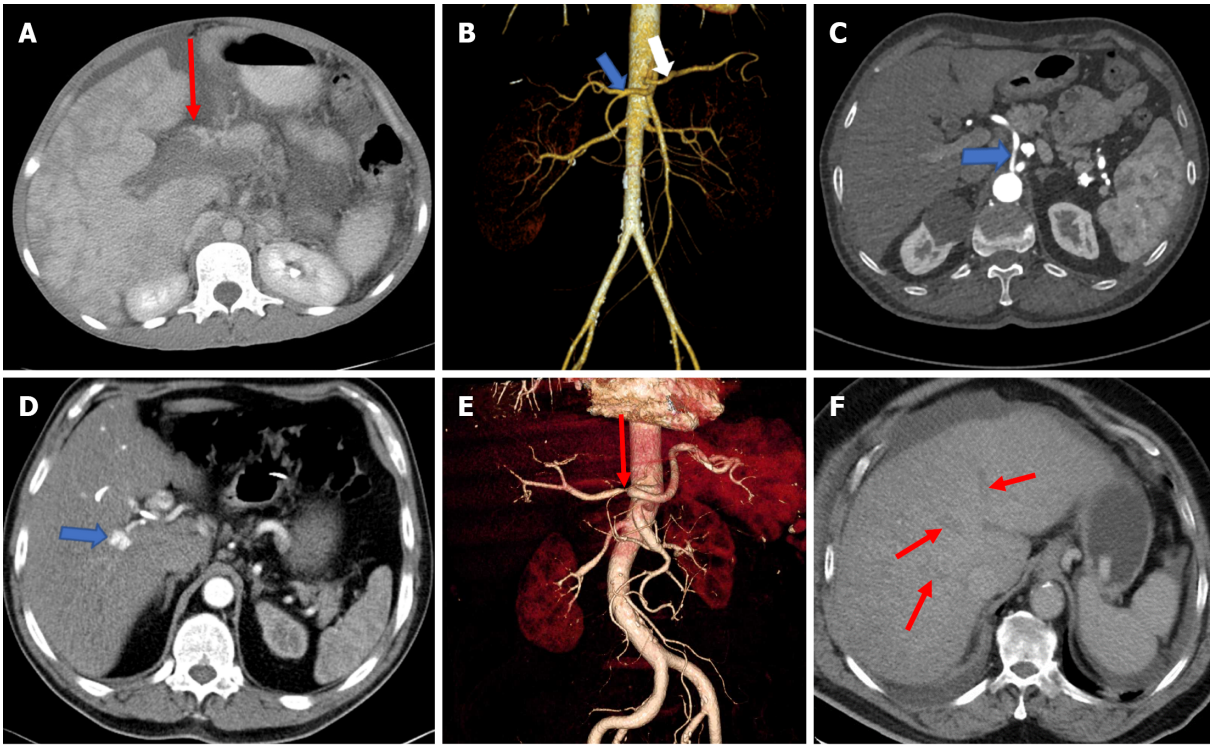

DOI: 10.4329/wjr.v15.i1.1 **Copyright** ©The Author(s) 2023.

Figure 1 Image examination. A: Axial computed tomography (CT) shows portal vein thrombosis; B: Separate origins of the common hepatic artery and the splenic artery. Coronal volume rendered image of a 44-year-old female presenting with right lumber pain demonstrates a hepatic arterial variation as the common hepatic artery (blue arrow) and the splenic artery (white arrow) originating directly from the abdominal aorta separately; C: The common hepatic artery directly originating from the abdominal aorta. Axial contrast-enhanced CT of a 55-year-old male patient with known peripheral vascular disease presenting direct origin of the common hepatic artery (arrow) from the abdominal aorta; D: Hepatic artery pseudoaneurysm. Axial contrast-enhanced arterial phase CT image of a 42-year-old man, suffering from epigastric pain and presenting with hemobilia and elevated liver enzymes, shows an 8 mm diameter pseudoaneurysm (arrow); E: High grade stenosis of the common hepatic artery. Coronal volume rendered CT image of a 76-year-old male with the diagnosis of vasculitis demonstrates severe stenosis (arrow); F: Occlusion of all hepatic veins consistent with Budd-Chiari syndrome. Venous phase axial CT scan shows thrombosed hepatic veins (arrows).

or stenosis of hepatic arterial flow does not generally result in parenchymal infarction (Figure 1E). CTA is the most commonly utilized modality to demonstrate localization and severity of the abrupt vessel. A wedge-shaped low-attenuation area in the liver periphery can be observed when hepatic infarctions are caused by hepatic artery flow disturbances. Central liver infarcts are characterized by a round-shaped lesion instead of wedge-shaped[18]. Vascular complications following liver transplantation include hepatic artery thrombosis occurring in 2%-5% of cases and stenosis occurring in 5%-11%, which may lead to irreversible infarctions and loss of the liver graft[19,20]. Hepatic artery dissection may occur

spontaneously and/or following liver transplants. Hypertension and preexisting vascular disease prior to surgery may be related with spontaneous dissection[21]. Hepatic artery aneurysms represent 20% of all visceral aneurysms. They usually have an extrahepatic location at the level of common hepatic or right hepatic arteries and common etiologies are trauma, tumors, infection, and iatrogenic reasons[22]. CT is an excellent diagnostic tool in which aneurysm appears as a fusiform dilatation of the vessel lumen, as well-defined focal enhancing lesions that may simulate hypervascular tumours[18]. Hepatic artery pseudoaneurysms (Figure 1D) differ from true aneurysms with the appearance of more irregular peripheral margins[22]. Hepatic arterio-portal shunts (HAPS) occur due to fistulization of blood flow from the hepatic artery to the portal vein. HAPS are frequently asymptomatic. However, systemic complications may arise including the development of portal hypertension, as well as accelerated metastasis in patients with malignant tumors. HAPS is divided into three types according to the anatomic location of the shunt within the liver: (1) Central HAPS: When the shunt is located in the porta hepatis, such central HAPS is manifested as earlier enhancement and arterial-phase opacification of the central portal veins during CT scanning; (2) Peripheral HAPS: When the shunt is located in peripheral liver parenchyma. Given the smaller hepatic vascular size in this region, early contrast into the portal veins generally does not occur. Shunts in this region of the liver usually manifest as transient hepatic enhancement differences; and (3) mixed HAPS: Alternatively, HAPS may demonstrate both central and peripheral findings[22]. Abnormal vessels that arise from the hepatic arteries promptly opacify the liver, thereby giving rise to the characteristic blush of an arteriovenous shunt.

Lymphatics of the liver

The liver is the largest lymph-producing organ, accounting for 25%-50% of lymph passing through the thoracic duct[23]. The hepatic lymphatic system transport lymph through lymphatic vessels to draining lymph nodes to remove waste products and immune cells. Sinusoids are covered by fenestrated liver sinusoidal endothelial cells (LSECs). Hepatic lymphatic fluid originates mainly from plasma components filtered through the fenestrae of LSECs and flows into the space of Disse. In this tight space between the hepatocytes and the sinusoid, fluid and solid materials pass through. The space of Disse cannot be observed by biopsy and is mainly occupied by reticular arcuate fibers. Especially during passive hepatic congestion, anoxia, or in some toxic conditions resulting from hepatic edema, we observe a dilatation of this perisinusoidal space filled with protein-rich fluid. These spaces have contact with the periportal spaces (space of Mall) between the stroma of the portal tract and the outermost hepatocytes. The lymphatic fluid inside the perisinusoidal and periportal spaces drains into the lymphatics in the portal triad. A rich lymphatic network is also shown around the bile ducts, reaching under the epithelium. There may also be very thin lymphatic vessels accompanying arterioles in the parenchyma. In addition, under the Glisson capsule, there is a subperitoneal lymph drainage communicating with both the lymphatics in the gallbladder bed and the parenchymal lymph vessels. The lymphatic vessels in the portal triad take different routes: Most of them first travel to the hepatic lymph nodes and drain into the coeliac lymph nodes and the lymph nodes around the cisterna chyli; some reach the thoracic duct directly from the porta hepatis; some drain into the lymph nodes around the inferior vena cava. The subcapsular lymphatics drain to the lymph nodes around the inferior vena cava and the diaphragmatic hiatus and then reach the thoracic duct directly. Lymphatics coming from the left side of the posterior surface of the liver drain into the paracardial group of the left gastric lymph nodes, and those coming from the right side directly into the coeliac lymph nodes. Although the lymph from the gallbladder and extrahepatic bile ducts mostly drains into the hepatic lymph nodes, a few vessels from the common hepatic duct go to the pyloric lymph nodes. Normally, hepatic lymph vessels do not anastomose with duodenal and pancreatic lymph vessels. A significant increase in the number of lymphatic vessels (lymphangiogenesis) has been reported in various pathological conditions of the liver, including cirrhosis, viral hepatitis, lymphedema, cholestasis, portal hypertension, biliary cholangitis, and hepatocellular carcinoma[23-29].

Hepatic vein

Most of the venous blood of the liver is drained by the three main hepatic veins (RHV, LHV, and intermediate hepatic vein), which open into the suprahepatic part of the superior vena cava. Numerous small hepatic veins open into the intrahepatic portion (at the sulcus for the inferior vena cava) of the inferior vena cava. The RHV drains liver segments V-VII, the middle hepatic vein (MHV) drains segments IV, V, VIII, and the LHV drains segments II and III[3]. Impairment of the hepatic venous outflow can be catastrophic. Patients may experience rapid onset jaundice and severe ascites. The increased intrahepatic pressure, caused by the inability of the massive blood flow into the liver, causes severe centrilobular congestion and subsequent parenchymal necrosis. This clinical condition of hepatic venous outflow obstruction is called the Budd-Chiari syndrome (BCS) (Figure 1F)[18]. This definition excludes the outflow impairment that results from heart failure or pericardial diseases. The definition also excludes sinusoidal obstruction syndrome. The compromised hepatic venous flow results in dramatically increased sinusoidal pressure that reverses hepatic drainage into the portal venous system. In approximately 75% of the cases, a hematologic abnormality or an underlying thrombotic diathesis can be identified[30,31]. CT clearly shows the obstructed hepatic veins and associating parenchymal changes[32]. The absence of contrast enhancement in the hepatic vein is the pathognomonic imaging

findings on CT[12]. In the acute phase, the liver becomes enlarged with smooth contours and appears heterogeneously edematous with parenchymal perfusion abnormalities with the decreased flow in the liver periphery and enhanced flow in the central liver parenchyma in the hepatic arterial phase. Patchy and decreased contrast enhancement in the liver periphery, in the arterial phase, results from edema and congestion in the peripheral regions due to flow stasis in portal vein branches and the liver sinusoids[12,19,33]. This finding is related to elevated post-sinusoidal pressure[33]. A heterogeneous and mottled mosaic pattern of parenchymal enhancement can also be encountered in congestive hepatopathy. Congestion is due to passive stasis of blood within the liver parenchyma secondary to impaired hepatic venous outflow due to decompensated cardiac disease[18,31]. Visualization of patency of hepatic veins and inferior vena cava differentiates congestive hepatopathy from BCS. A mosaic pattern of enhancement with linear and curvilinear areas of poor enhancement is seen in the portal venous phase images, described as nutmeg liver. A "flip-flop" pattern may occur in the portal venous phase as the central part of the liver demonstrates low attenuation due to contrast wash-out and gradual increase of the peripheral attenuation. The caudate lobe may demonstrate better venous enhancement due to its unique venous drainage pattern[32]. Associated features of cardiac dysfunction aid diagnosis [18].

The vascular variants that are of surgical importance include variants of the hepatic vein also: (1) An accessory RHV occurs in 52.5% of patients; (2) two accessory hepatic veins in 12%; (3) an accessory vein draining the caudate lobe in 12%; (4) an accessory inferior RHV; and (5) early branching of the vein that drains the right superoanterior segment (segment VIII) into the MHV.

Significant hepatic venous variants affecting both donors and recipients are seen in approximately 30% of patients, thus presenting a problem for the surgeon, and may result in a modification of the hepatectomy plane[34].

CONCLUSION

CTA may slightly be favourable in hepatic vascular disorders due to being time saving in critically ill patients with distended abdomen and pain. For a complete mapping of the hepatic vasculature, CT scan is preferable to other imaging modalities. Correct diagnosis and proper intervention are crucial for appropriate clinical management. CTA is an effective, high-resolution, noninvasive imaging technique that demonstrates the presence of vascular pathology, with a direct impact on treatment decisions including patient selection for surgical management. Also, the objective of vascular imaging in patients with liver neoplasms is to provide a vascular map for understanding the relationship of the tumor to adjacent vessels, which is needed for tumor resection that includes a peripheral tumor-free margin. Multiplanar reformation and 3D reconstruction are very helpful in demonstrating the relationship of liver tumors to the hepatic veins and inferior vena cava. Awareness of the imaging findings of hepatic vascularization is crucial for the correct diagnosis and optimization of the treatment to avoid complications.

FOOTNOTES

Author contributions: Firat A and Balaban YH designed, wrote, and finally edited the paper; Firat A and Abbasoglu TT analyzed and interpreted the data; Karcaaltincaba M and Balaban YH performed the clinical interventions and made critical revisions to the manuscript.

Conflict-of-interest statement: The authors declare that they have no conflict of interest to disclose.

Country/Territory of origin: Turkey

ORCID number: Aysegul Firat 0000-0001-5105-0057; Tugce Taskindere Abbasoglu 0000-0003-2747-417X; Musturay Karcaaltincaba 0000-0002-3384-0909; Yasemin H Balaban 0000-0002-0901-9192.

S-Editor: Chen YL
L-Editor: Wang TQ
P-Editor: Chen YL

REFERENCES

1 **Colagrande S**, Centi N, La Villa G, Villari N. Transient hepatic attenuation differences. *AJR Am J Roentgenol* 2004; **183**: 459-464 [PMID: 15269041 DOI: 10.2214/ajr.183.2.1830459]
2 **Price M**, Patino M, Sahani D. Computed Tomography Angiography of the Hepatic, Pancreatic, and Splenic Circulation. *Radiol Clin North Am* 2016; **54**: 55-70 [PMID: 26654391 DOI: 10.1016/j.rcl.2015.08.009]
3 **Standring S**. Gray's Anatomy The Anatomical Basis of Clinical Practice. 42nd ed. London: Churchill Livingstone Elsevier, 2021: 327-329, 1205-1217
4 **Gissen P**, Arias IM. Structural and functional hepatocyte polarity and liver disease. *J Hepatol* 2015; **63**: 1023-1037 [PMID: 26116792 DOI: 10.1016/j.jhep.2015.06.015]
5 **Sun P**, Zhang G, Su X, Jin C, Yu B, Yu X, Lv Z, Ma H, Zhang M, Wei W, Li W. Maintenance of Primary Hepatocyte Functions In Vitro by Inhibiting Mechanical Tension-Induced YAP Activation. *Cell Rep* 2019; **29**: 3212-3222.e4 [PMID: 31801084 DOI: 10.1016/j.celrep.2019.10.128]
6 **Erwin K**, Hans-Dieter K. Hepatology: Textbook and Atlas. 3rd ed. Heidelberg: Springer Medizin Verlag, 2008: 26-28
7 **William KO**, Patrick CN. Netter's Essential Histology. 2nd ed. Philadelphia: Elsevier Sauders, 2013: 314-316
8 **Schmidt S**, Demartines N, Soler L, Schnyder P, Denys A. Portal vein normal anatomy and variants: implication for liver surgery and portal vein embolization. *Semin Intervent Radiol* 2008; **25**: 86-91 [PMID: 21326549 DOI: 10.1055/s-2008-1076688]
9 **DeLeve LD**, Valla DC, Garcia-Tsao G; American Association for the Study Liver Diseases. Vascular disorders of the liver. *Hepatology* 2009; **49**: 1729-1764 [PMID: 19399912 DOI: 10.1002/hep.22772]
10 **Chawla Y**, Duseja A, Dhiman RK. Review article: the modern management of portal vein thrombosis. *Aliment Pharmacol Ther* 2009; **30**: 881-894 [PMID: 19678814 DOI: 10.1111/j.1365-2036.2009.04116.x]
11 **Onur MR**, Karaosmanoglu AD, Akca O, Ocal O, Akpinar E, Karcaaltincaba M. Imaging features of non-traumatic vascular liver emergencies. *Jpn J Radiol* 2017; **35**: 215-224 [PMID: 28243837 DOI: 10.1007/s11604-017-0624-0]
12 **Gallego C**, Velasco M, Marcuello P, Tejedor D, De Campo L, Friera A. Congenital and acquired anomalies of the portal venous system. *Radiographics* 2002; **22**: 141-159 [PMID: 11796904 DOI: 10.1148/radiographics.22.1.g02ja08141]
13 **Bazan F**, Busto M. IMAGES IN CLINICAL MEDICINE. Pylephlebitis as a Complication of Diverticulitis. *N Engl J Med* 2015; **373**: 2270 [PMID: 26630145 DOI: 10.1056/NEJMicm1501584]
14 **Kanellopoulou T**, Alexopoulou A, Theodossiades G, Koskinas J, Archimandritis AJ. Pylephlebitis: an overview of non-cirrhotic cases and factors related to outcome. *Scand J Infect Dis* 2010; **42**: 804-811 [PMID: 20735334 DOI: 10.3109/00365548.2010.508464]
15 **Turner KC**, Bohannon WT, Atkins MD. Portal vein aneurysm: a rare occurrence. *J Vasc Nurs* 2011; **29**: 135-138 [PMID: 22062791 DOI: 10.1016/j.jvn.2011.08.001]
16 **Michels NA**. Blood supply and anatomy of the upper abdominal organs with a descriptive atlas. Philadelphia: Lippincott, 1955: 64-69
17 **Favelier S**, Germain T, Genson PY, Cercueil JP, Denys A, Krausé D, Guiu B. Anatomy of liver arteries for interventional radiology. *Diagn Interv Imaging* 2015; **96**: 537-546 [PMID: 24534562 DOI: 10.1016/j.diii.2013.12.001]
18 **Virmani V**, Ramanathan S, Virmani VS, Kielar A, Sheikh A, Ryan J. Non-neoplastic hepatic vascular diseases: spectrum of CT and MRI appearances. *Clin Radiol* 2014; **69**: 538-548 [PMID: 24581966 DOI: 10.1016/j.crad.2013.12.017]
19 **Khalaf H**. Vascular complications after deceased and living donor liver transplantation: a single-center experience. *Transplant Proc* 2010; **42**: 865-870 [PMID: 20430192 DOI: 10.1016/j.transproceed.2010.02.037]
20 **Hwang JY**, Kim KW, Lee SJ, Kim SY, Lee JS, Kim HJ, Lee J, Song GW, Lee SG. The computed tomographic angiography finding of hepatic artery dissection after living donor liver transplantation; what is the clinical significance? *Clin Imaging* 2016; **40**: 130-136 [PMID: 26271148 DOI: 10.1016/j.clinimag.2015.06.007]
21 **Müller MF**, Kim D. Spontaneous dissection of the hepatic artery. *Abdom Imaging* 1995; **20**: 462-465 [PMID: 7580786 DOI: 10.1007/BF01213273]
22 **O'Driscoll D**, Olliff SP, Olliff JF. Hepatic artery aneurysm. *Br J Radiol* 1999; **72**: 1018-1025 [PMID: 10673957 DOI: 10.1259/bjr.72.862.10673957]
23 **Tanaka M**, Iwakiri Y. The Hepatic Lymphatic Vascular System: Structure, Function, Markers, and Lymphangiogenesis. *Cell Mol Gastroenterol Hepatol* 2016; **2**: 733-749 [PMID: 28105461 DOI: 10.1016/j.jcmgh.2016.09.002]
24 **Wang Q**, Koniaris LG, Milgrom DP, Patel A, Hu M, Cui E, Deng Y, Akisik F. CT and MRI imaging and interpretation of hepatic arterioportal shunts. *Transl Gastroenterol Hepatol* 2019; **4**: 34 [PMID: 31231701 DOI: 10.21037/tgh.2019.05.05]
25 **Chung C**, Iwakiri Y. The lymphatic vascular system in liver diseases: its role in ascites formation. *Clin Mol Hepatol* 2013; **19**: 99-104 [PMID: 23837133 DOI: 10.3350/cmh.2013.19.2.99]
26 **Thelen A**, Jonas S, Benckert C, Weichert W, Schott E, Bötcher C, Dietz E, Wiedenmann B, Neuhaus P, Scholz A. Tumor-associated lymphangiogenesis correlates with prognosis after resection of human hepatocellular carcinoma. *Ann Surg Oncol* 2009; **16**: 1222-1230 [PMID: 19224279 DOI: 10.1245/s10434-009-0380-1]
27 **Oikawa H**, Masuda T, Sato S, Yashima A, Suzuki K, Satodate R. Changes in lymph vessels and portal veins in the portal tract of patients with idiopathic portal hypertension: a morphometric study. *Hepatology* 1998; **27**: 1607-1610 [PMID: 9620334 DOI: 10.1002/hep.510270621]
28 **Yamauchi Y**, Michitaka K, Onji M. Morphometric analysis of lymphatic and blood vessels in human chronic viral liver diseases. *Am J Pathol* 1998; **153**: 1131-1137 [PMID: 9777944 DOI: 10.1016/s0002-9440(10)65657-x]
29 **Soyer P**, Heath D, Bluemke DA, Choti MA, Kuhlman JE, Reichle R, Fishman EK. Three-dimensional helical CT of intrahepatic venous structures: comparison of three rendering techniques. *J Comput Assist Tomogr* 1996; **20**: 122-127 [PMID: 8576462 DOI: 10.1097/00004728-199601000-00023]
30 **Cura M**, Haskal Z, Lopera J. Diagnostic and interventional radiology for Budd-Chiari syndrome. *Radiographics* 2009; **29**: 669-681 [PMID: 19448109 DOI: 10.1148/rg.293085056]
31 **Valla DC**, Cazals-Hatem D. Vascular liver diseases on the clinical side: definitions and diagnosis, new concepts. *Virchows*

Arch 2018; **473**: 3-13 [PMID: 29572606 DOI: 10.1007/s00428-018-2331-3]

32 **Karaosmanoglu AD**, Uysal A, Akata D, Ozmen MN, Karcaaltincaba M. Role of imaging in visceral vascular emergencies. *Insights Imaging* 2020; **11**: 112 [PMID: 33057847 DOI: 10.1186/s13244-020-00913-3]

33 **Torabi M**, Hosseinzadeh K, Federle MP. CT of nonneoplastic hepatic vascular and perfusion disorders. *Radiographics* 2008; **28**: 1967-1982 [PMID: 19001652 DOI: 10.1148/rg.287085067]

34 **Sahani D**, Mehta A, Blake M, Prasad S, Harris G, Saini S. Preoperative hepatic vascular evaluation with CT and MR angiography: implications for surgery. *Radiographics* 2004; **24**: 1367-1380 [PMID: 15371614 DOI: 10.1148/rg.245035224]

World Journal of Radiology

Submit a Manuscript: https://www.f6publishing.com

World J Radiol 2023 January 28; 15(1): 10-19

DOI: 10.4329/wjr.v15.i1.10

ISSN 1949-8470 (online)

MINIREVIEWS

Advancements of molecular imaging and radiomics in pancreatic carcinoma

Xiao-Xi Pang, Liang Xie, Wen-Jun Yao, Xiu-Xia Liu, Bo Pan, Ni Chen

Specialty type: Oncology

Provenance and peer review: Invited article; Externally peer reviewed.

Peer-review model: Single blind

Peer-review report's scientific quality classification
Grade A (Excellent): 0
Grade B (Very good): B
Grade C (Good): C
Grade D (Fair): 0
Grade E (Poor): 0

P-Reviewer: Chisthi MM, India; Wu CQ, China

Received: September 30, 2022
Peer-review started: September 30, 2022
First decision: October 29, 2022
Revised: November 12, 2022
Accepted: January 9, 2023
Article in press: January 9, 2023
Published online: January 28, 2023

Xiao-Xi Pang, Liang Xie, Xiu-Xia Liu, Department of Nuclear Medicine, The Second Hospital of Anhui Medical University, Hefei 230601, Anhui Province, China

Wen-Jun Yao, Department of Radiology, The Second affiliated hospital of Anhui Medical University, Hefei 230601, Anhui Province, China

Bo Pan, PET/CT Center, The First Affiliated Hospital of USTC, Division of Life Sciences and Medicine, University of Science and Technology of China, Hefei 230001, Anhui Province, China

Ni Chen, Department of Nuclear Medicine, School of Basic Medicine Anhui Medical University, Hefei 230032, Anhui Province, China

Corresponding author: Ni Chen, Department of Nuclear Medicine, School of Basic Medicine Anhui Medical University, No. 81 Meishan Road, Hefei 230032, Anhui Province, China. icefei@mail.ustc.edu.cn

Abstract

Despite the recent progress of medical technology in the diagnosis and treatment of tumors, pancreatic carcinoma remains one of the most malignant tumors, with extremely poor prognosis partly due to the difficulty in early and accurate imaging evaluation. This paper focuses on the research progress of magnetic resonance imaging, nuclear medicine molecular imaging and radiomics in the diagnosis of pancreatic carcinoma. We also briefly described the achievements of our team in this field, to facilitate future research and explore new technologies to optimize diagnosis of pancreatic carcinoma.

Key Words: Pancreatic carcinoma; Magnetic resonance imaging; Molecular imaging; Positron emission tomography-computed tomography; Positron emission tomography-magnetic resonance; Artificial intelligence

Core Tip: Pancreatic carcinoma remains high incidence and poor prognosis. Molecular imaging enables early and precise diagnosis, efficient assessment, non-invasive pathological classification. This paper aims to review the recent research progress of nuclear medicine, magnetic resonance imaging and radiomics in the diagnosis of pancreatic carcinoma, and also briefly describe our team's work in this field.

Citation: Pang XX, Xie L, Yao WJ, Liu XX, Pan B, Chen N. Advancements of molecular imaging and radiomics in pancreatic carcinoma. *World J Radiol* 2023; 15(1): 10-19
URL: https://www.wjgnet.com/1949-8470/full/v15/i1/10.htm
DOI: https://dx.doi.org/10.4329/wjr.v15.i1.10

INTRODUCTION

In the past decade, significant progress has been made in the medical technology for the treatment of cancers. However, the prognosis of pancreatic carcinoma remains extremely poor due to its insidious location, high malignancy, easy metastasis and rapid progression, which increases the difficulty of early and accurate assessment. Radical surgical resection rate of pancreatic cancer patients is less than 20%. Pancreatic carcinoma is also resistant to radiotherapy and chemotherapy. Moreover, targeted drug therapy, and cytotoxic T-lymphocyte-associated protein 4 and programmed death-1/programmed death-ligand 1 antibody immunotherapy are ineffective. The five-year survival rate of patients remains below 5%-9%, and the number of deaths is the fourth highest among malignant tumors[1]. Early and accurate diagnosis as well as efficacious assessment of pancreatic carcinoma have important clinical significance.

Conventional imaging techniques makes important significance in theranostic of pancreatic cancer; however, these technologies are still deficiencies yet. First of all, magnetic resonance (MR) and computed tomography (CT) only detects limited range with regional scan in clinical routine diagnosis of pancreatic carcinoma, therefore, many patients with distant metastasis are misdiagnosed or never diagnosed. Secondly, the rate of misdiagnosis was high in lymphatic metastasis by MR and CT scan. By reason of no static image provided, ultrasound examination is very unfavorable for reading in clinical work, even this method has the double advantage of real time imaging and radiation lessness. What's more, ultrasound is affected greatly by operators. Finally, some patients who cannot have a proper assessment in regional lymphatic metastasis, especially patients after chemotherapy, even whole body ^{18}F-FDG positron emission tomography (PET)/CT scan.

Molecular imaging has advanced rapidly in recent years. It enables early and precise diagnosis, efficacy assessment, non-invasive pathological classification, and acts as an important "bridge" to achieve precise diagnosis and treatment[2]. It can meet clinical demands and better protect patient privacy compared to genetic testing. This paper aimed to review the recent research progress of nuclear medicine, magnetic resonance imaging, molecular imaging and radiomics in the diagnosis and treatment of pancreatic carcinoma, and also briefly describe our team's work in this field.

NUCLEAR MEDICINE MOLECULAR IMAGING

Nuclear medicine molecular imaging is based on the principle of injecting microscopic molecular probes into the body and selectively targeting them to appropriate sites based on different properties, in order to qualify or quantify organs, tissues or lesions for assessing diseases at the molecular level. Molecular imaging in nuclear medicine has made significant advances in the treatment of pancreatic carcinoma in recent years.

Glucose metabolism imaging

^{18}F-FDG is a glucose analogue, which is rapidly taken up by the glucose-transporter on the cell surface after intravenous injection. Various tumor cells, including pancreatic carcinoma, and inflammatory cells in the tumor microenvironment absorb a large amount of ^{18}F-FDG, but the uptake is influenced by various conditions and the underlying mechanisms are complex[3].

^{18}F-FDG PET/CT has high specificity, accuracy and sensitivity in the diagnosis of pancreatic carcinoma, and has important clinical value in the diagnosis, staging, surgical indication and evaluation efficacy of pancreatic carcinoma[4]. ^{18}F-FDG PET/CT is more sensitive and accurate than CT in detecting tumor metastasis, and its whole-body scan is beneficial for tumor staging[5]. This technique detected distant metastases in about one-third of pancreatic carcinoma patients and changed the staging of approximately 26.8% of patients[6]. Its standardized uptake value (SUV) quantification and the rate of change were significantly correlated with tumor size[7], malignancy[8], vascular invasion[9], and lymph node metastasis. In addition, ^{18}F-FDG PET has significant value in efficacy assessment[10] and survival

prediction[11]. For example, the patients with baseline SUV < 3.5 (and/or) SUV decrease ≥ 60% had better overall survival (OS) and progression-free survival (PFS)[12]. In locally advanced or metastatic pancreatic carcinoma, the PFS of patients with SUV_{max} < 6.8 was significantly longer than that of patients with SUV_{max} ≥ 6.8[13]. ^{18}F-FDG PET/CT-guided radiotherapy with metabolic tumor volume and total lesion glycolysis (TLG) can be used as independent factors affecting prognosis[14]. Yamamoto *et al*[15] found that the early postoperative recurrence rate of pancreatic carcinoma in patients with SUV_{max} ≥ 6.0 was higher than that of patients with SUV_{max} < 6.0, and median OS of the former was lower than the latter (Table 1)[16].

With the increasing application of ^{18}F-FDG PET/CT in recent years, several shortcomings have been gradually revealed. First, as a non-tumor-specific imaging agent, ^{18}F-FDG PET reflects glucose metabolism and is not directly related to the biological properties of the tumor. So non-neoplastic lesions such as inflammation, tuberculosis, or even non-specific uptake with increased glucose metabolism can lead to false positive results. Second, if the patient has high blood glucose levels, uses short-acting insulin or exercises, ^{18}F-FDG can also lead to reduced sensitivity due to increased background uptake. In order to address these problems, nuclear medicine researchers have developed a series of more specific imaging agents for different targets.

Non-glucose metabolism imaging

The highly specific non-FDG molecular probes with different targets achieve accurate diagnosis of pancreatic carcinoma, and also enable non-invasive visualization of the expression of different receptors in tumors, facilitating individualized precision medicine. These imaging agents have been particularly successful in imaging of integrin receptor, somatostatin receptor, tumor-associated fibroblasts, *etc*. Our team has also conducted in-depth research on PD-L1-targeted imaging, non-radioactive molecular imaging and highly specific targeted radiotherapy.

Somatostatin receptor imaging

Somatostatin receptor imaging is mainly used in pancreatic neuroendocrine tumors, with sensitivity of 86%-100% and specificity of 79%-100%[17]. The precursors of somatostatin receptor (SSTR) imaging agents are mainly Tyr(3)-octreotate, 1-Nal(3)-octreotide and D-Phe1-Tyr(3)-octreotide, which have different affinities for different somatostatin receptor subtypes[17]. The neuroendocrine tumors with high differentiation (G1-G2, Ki-67 < 10%) generally showed high expression of SSTR and positive SSTR imaging. Moreover, the degree of malignancy was low, the level of glycolysis was decreased, and the metabolism of FGD was only slightly increased or defective, which led to low sensitivity of ^{18}F-FDG PET [18,19]. In contrast, due to the loss of SSTR and negative SSTR imaging, the increase of malignant degree led to increased glycolysis[20], high metabolism of FGD and increased sensitivity of ^{18}F-FDG PET/CT. In addition to the above three SSTR agonists, SSTR inhibitors have other advantages such as several binding sites, low degradation rate and longer retention in tumors[21] (Table 2)[17].

Fibroblast activation protein imaging

Cancer-associated fibroblasts (CAFs) are a major component of the mesenchyme surrounding epithelial cancer cells. Fibroblast activating protein (FAP) is a marker of CAFs. It is highly expressed in tumor stromal fibroblasts of most common human epithelial carcinomas, and has lower expression in normal tissues[22]. CAFs can form physical and metabolic barriers, which is partly responsible for the resistance of pancreatic carcinoma to chemotherapy and radiotherapy, by reducing the therapeutic effect of combined chemotherapy on pancreatic carcinoma[23]. High expression of CAFs in pancreatic carcinoma is associated with shorter OS and disease-free survival[24,25].

At present, the commonly used FAP-targeted imaging agents are various radionuclide-labeled small molecular FAP inhibitors (FAPIs), mainly FAPI-04, FAPI-21 and FAPI-46. The commonly used imaging agent ^{68}Ga/^{18}F-labeled FAPI-04 shows a significantly high uptake in pancreatic carcinoma, which has a good diagnostic efficacy for the primary focus of pancreatic carcinoma. In a comparative study of pancreatic carcinoma and pancreatitis, ^{68}Ga-FAPI-04 PET/MR and ^{18}F-FDG PET/CT positive rates were both 100%, but the former SUV_{max} was significantly higher than the latter SUV_{max} (P < 0.05). In addition, ^{68}Ga-FAPI-04 could detect more lymph node metastases, but ^{18}F-FDG was able to detect more liver metastases than ^{68}Ga-FAPI-04[26]. ^{68}Ga-FAPI-04 may be superior to ^{18}F-FDG and CT in the diagnosis of lymph node, bone, liver, lung, peritoneal and pleural metastases of pancreatic carcinoma[27,28]. Deng *et al*[29] reported a 65-year-old male patient with pancreatic head cancer and liver metastasis. ^{18}F-FDG showed slight uptake in the pancreatic lesions and the tenth rib on the right, but not in many low-density or isodensity nodules in the liver, while ^{68}Ga-FAPI PET/CT showed strong FAPI uptake in the pancreatic lesions and the tenth rib on the right, as well as multiple liver lesions.

Our team conducted a comparative study of FAPI and FDG imaging of pancreatic cancer (Figure 1), and redesigned FAPI based on new ideas, which is expected to exceed the existing FAPI-04, FAPI-21 and FAPI-46 in imaging and therapeutic effects. At present, chemical synthesis has been completed and radionuclides such as iodine and technetium have been labeled, and further cellular and animal experiments will be conducted soon.

Table 1 Summary of sensitivity and specificity of different imaging modalities for the diagnosis of pancreatic cancer[16]

Year	Study type	Pancreatic cancer–all (*n*)	^{18}F-FDG PET-CT		CT		MRI		EUS	
			Sens	Spec	Sens	Spec	Sens	Spec	Sens	Spec
2016	Retrospective study	139-139	0.78	–	0.76	–	–	–	–	–
2014	Retrospective study	33–52	1	0.9	0.92	0.5	0.89	0.75	1	0.88
2009	Meta-analysis	3857[1]	0.9	0.8	–	–	–	–	0.81	0.93
2017	Meta-analysis	3567–5399	0.89	0.7	0.9	0.87	0.93	0.89	0.91	0.86
2014	Retrospective study	80–91	0.68	0.73	–	–	–	–	–	–
2018	Prospective study	278–583	0.93	0.76	0.89	0.71	–	–	–	–
2015	Retrospective study	50–70	0.92	0.65	0.82	0.65	–	–	–	–

[1]The study included a total of 3857 patients, but we were unable to obtain the specific number of pancreatic cancer.
This table is adopted from[16]. Sens: Sensitivity, Spec: Specificity. PET: Positron emission tomography; CT: Computed tomography; MRI: Magnetic resonance imaging; EUS: Endoscopic ultrasound.

Table 2 Summary of the main clinical key points of the two EANM/ENETS recommended radiopharmaceuticals[17]

Clinical key points			
Radiopharmaceuticals	**Main indication**	**Diagnostic accuracy**	**False positive findings**
^{68}Ga-TATE, TOC, NOC	Staging and restaging any non-insulinoma panNET case; detection of the unknown primary tumour site or early relapse; evaluation in-vivo SRE; selection for PRRT and/or cold SSA	Sensitivity: 86% to 100%; specificity: from 79% to 100%	Pancreatic uncinate process, accessory spleens (including intra-pancreatic, splenules, infectious/inflammatory findings, non-neuroendocrine tumours)
^{18}F-FDG	High grade G2, G3 and NEC; prognosis; rapid tumour progression in earlier diagnosed G1–G2 tumours	Sensitivity: 40% in G1, 60% in G2; 95% in G3 patients	Infectious/inflammatory findings, non-neuroendocrine tumours

This table is adopted from[17]. TATE: Tyr(3)-octreotate; NOC: 1-Nal(3)-octreotide; TOC: D-Phe1-Tyr(3)-octreotide; NEC: Neuroendocrine carcinomas.

Integrin receptor imaging

Tumor neovascularization (angiogenesis) is necessary for maintaining the growth of malignant tumors, which plays a key role in tumor growth, invasion and metastasis, it is an important target for tumor diagnosis and treatment.

Integrin $\alpha v\beta_3$ receptor is an important component of the 24 integrins, which is highly expressed on the cell surface of tumor neovascular endothelial cells and many solid tumors. However, it has low or no expression in mature vascular endothelial cells and most normal tissues and organs in healthy people, and plays an important role in angiogenesis, metastasis and tumor invasion[30,31]. The integrin $\alpha v\beta_3$ receptor is highly expressed in about 60% of invasive pancreatic carcinomas, and the small polypeptide arginine glycine aspartic acid sequence (RGD) can be targeted to bind to $\alpha v\beta_3$ receptor. Using radionuclide-labeled RGD peptides, such as ^{111}In, ^{18}F, ^{68}Ga-labeled RGD, can be used to visualize and treat pancreatic carcinoma. Our research team has also studied RII and RIT based on molecular probes constructed by different radionuclide-labeled RGD and RRL peptides[32].

In addition to the integrin $\alpha v\beta_3$ receptor, integrin $\alpha V\beta_6$ is also highly expressed in pancreatic carcinoma[33]. Radiation molecular pancreatic probes constructed from the radionuclide ^{99m}Tc and ^{111}In-labeled HHK can target $\alpha v\beta_6$ with high specificity to achieve early diagnosis of pancreatic carcinoma and its metastases[34,35]. Based on previous studies, our research team redesigned the HHK peptide (Figure 2). The Gd-DOTA-HHK compound was obtained by chelating Gd^{3+}, which can achieve high specific enhancement of tumor $\alpha v\beta_6$ receptor during MRI T1WI scanning. Single photon emission CT imaging with high sensitivity and MRI with high soft tissue resolution combine perfectly to achieve high sensitivity and non-invasive visualization of $\alpha v\beta_6$ targets at high resolution.

In addition, some researchers have explored the application of radionuclide labeling dopa, Exendin-4, CXCR4, and PSMA in pancreatic carcinoma.

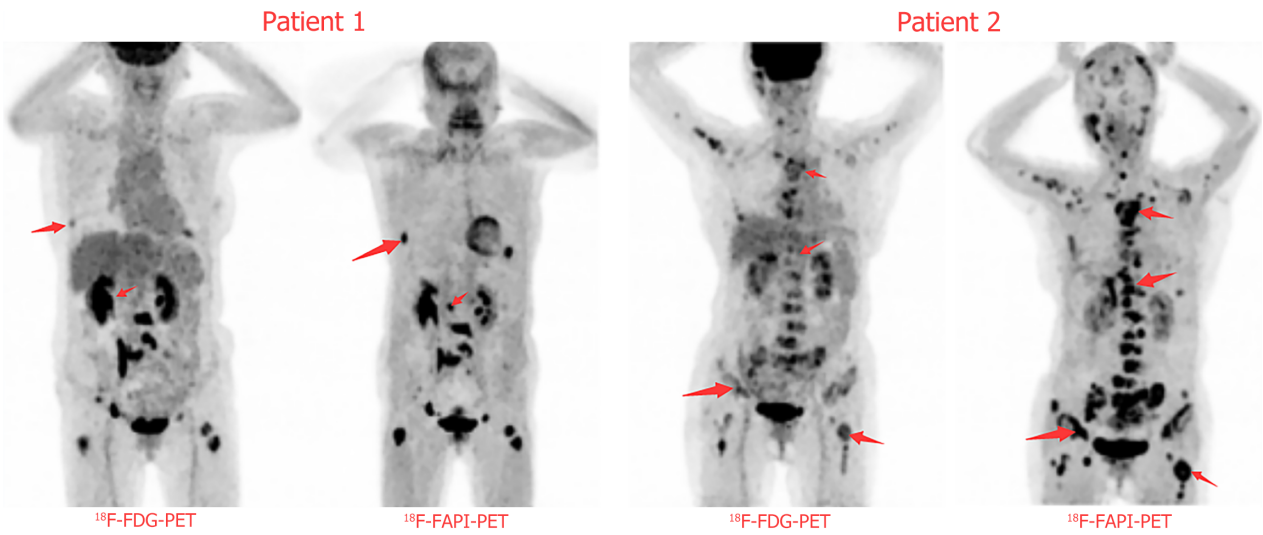

DOI: 10.4329/wjr.v15.i1.10 **Copyright** ©The Author(s) 2023.

Figure 1 Two patients with pancreatic cancer imaged with ^{18}F-FDG-positron emission tomography compared with ^{18}F-FAPI-positron emission tomography. Patient 1 was a 69-year-old female. Patient 2 was a 70-year-old female. ^{18}F-FAPI-positron emission tomography (PET) detected more lesions than ^{18}F-FDG-PET, and also had better contrast. PET: Positron emission tomography.

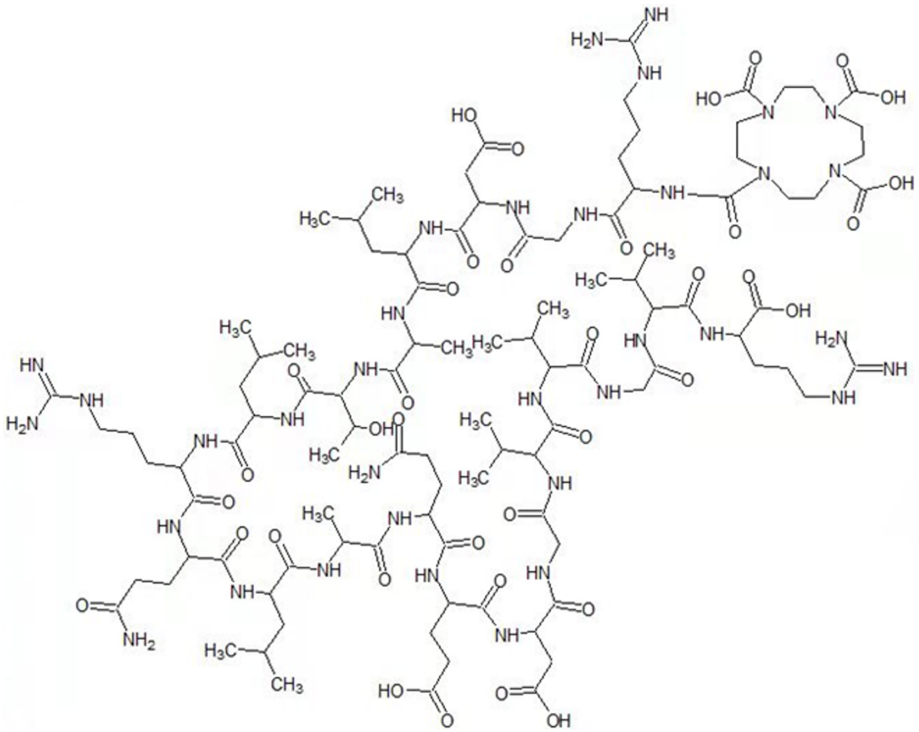

DOI: 10.4329/wjr.v15.i1.10 **Copyright** ©The Author(s) 2023.

Figure 2 Structure of the redesigned HHK peptide.

MAGNETIC RESONANCE MOLECULAR IMAGING

MRI utilizes magnetic resonance to obtain electromagnetic signals from the human body, which can be reconstructed by computer to show the different chemical components in the same tissue. Because MRI has the advantages of high soft tissue resolution, non-radiation, unrestricted imaging depth and multi-sequence imaging, and with the development of MRI-specific imaging agents, it is possible to evaluate lesions from multiple dimensions of functional and molecular images by MRI.

Diffusion-weighted imaging

Diffusion-weighted imaging (DWI) is the most widely used conventional MRI technique in addition to

T1WI and T2WI. The diffusion movement of water molecules reflects the microstructure of the tumor, such as internal cell density, extracellular space and heterogeneity. When the cell density increases, edema, fibrosis, *etc*., affect the cell membrane function, which can be detected due to enhanced signal.

Increased b-value (>1000 s/mm^2) DWI can increase lesion detection, but high b-value DWI images often exhibit low signal noise ratio, large diffusion-sensitive gradients that tend to distort images and longer scan times. The emergence of computed DWI has partially solved the above problem[36]. Liang *et al*[37] explored the value of computed DWI (cDWI) technique in the diagnosis of pancreatic carcinoma, and the results initially showed that a b-value of c1000-c1500 s/mm^2 at cDWI technique could effectively display pancreatic carcinoma as well as maintain the image quality. Compared to DWI, intravoxel incoherent motion imaging is based on a biexponential model, which can quantify the diffusion and perfusion motions of water molecules separately. It can reflect the diffusion and perfusion characteristics of tissue cells, respectively, and has the advantages of fast-imaging, low-noise, and multi-parameters[38].

MR dynamic enhancement/Perfusion imaging

MR enhanced or perfusion imaging facilitates T-staging of pancreatic carcinoma by observing the relationship between the lesion, its surrounding tissue and vascular invasion. Both dynamic contrast-enhanced MRI (DCE-MRI) and perfusion MRI can provide quantitative information on blood flow perfusion of lesions (such as tumor tissue)[39]. The most common forms include T2*-weighted dynamic susceptibility contrast (DSC) perfusion and T1-weighted DCE perfusion[40]. However, there are significant differences between the two imaging methods, PWI (DCE and DSC) can reflect the tumor microenvironment such as blood vessel density and blood flow state by quantitative and functional parameters, such as first transit time, mean transit time, time to peak, *etc*. while dynamic enhancement can only obtain time perfusion curves through multi-phase dynamic enhancement, but they are not molecular imaging *per se*.

MR targeted molecular imaging

The basic principle of MR targeted molecular imaging is similar to nuclear medicine molecular imaging. The first step is to construct a specific molecular probe, and then introduce it into the body. After the probe actively and specifically binds to the imaging target, the lesions containing specific molecular targets in the body will be imaged by MRI[41]. Due to the high specificity of the molecular probe, delayed scan time, continuous enhancement within the tumor and relatively high signal on T1WI during the delayed scan, the specificity of the diagnosis is greatly improved[42,43], which helps to improve the detection rate of early microscopic pancreatic carcinoma lesions.

MR molecular probes meet the requirements of high specificity, affinity and signal elements that can be detected by MRI, such as T1 contrast agent represented by gadolinium (Gd), manganese, zinc chelates (Positive) and T2 contrast agent represented by MNP (Negative). Gd is used as a signal component to synthesize paramagnetic molecular imaging probes, mainly to shorten the longitudinal relaxation time of hydrogen protons, increase the T1 relaxation rate and produce positive T1WI contrast [43]. The traditional Gd agent enhanced MRI is diagnosed by the hemodynamic characteristics of lack of blood supply in pancreatic carcinoma, with low relaxation rate and lack of tissue specificity[44]. In recent years, MNP, as represented by SPION, has been applied in MR molecular imaging studies, mainly to shorten the transverse relaxation time, improve the T2 relaxation rate and produce negative T2WI contrast. Compared with Gd and SPION, it has better magnetization and biocompatibility, and no risk of nephrogenic systemic fibrosis[45,46].

In recent years, MR molecular imaging of pancreatic carcinoma is mainly based on basic scientific research. At present, the main targets involved are SSTR[47], urokinase-type plasminogen activator receptor[48], insulin-like growth factor-1 receptor, $\alpha V\beta_6$, epidermal growth factor receptor, vascular endothelial growth factor receptor-2[49], *etc*., but their prospect of clinical application requires further study. In addition, targets such as reticulin-1 (plectin-1)[50], mucin-1[51], MUC4, carcinoembryonic antigen-related cell adhesion molecule 6[52], γ-glutamyltransferase 5[53], P32 protein[54], mesothelin [55], thymus fine cell differentiation antigen-1, cathepsin E, neutrophil gelatinase-associated lipid transport protein[56] were also examined, which could lead to a new imaging target for pancreatic carcinoma.

The slow progress of MR targeted molecular imaging compared to nuclear medicine molecular imaging is mainly due to its own limitations. First, the specificity of the above-mentioned types of targets is poor, which affects the specificity of MR molecular imaging[56]. Second, high concentrations of Gd molecular probes are required for imaging, which is difficult to achieve when some molecular targets are expressed at low levels. Finally, factors such as low blood supply, low perfusion in pancreatic carcinoma, denser stromal components in the tumor, and excessive uptake of the molecular probe by the reticuloendothelial system such as liver and spleen *in vivo* decrease the aggregation dose in the tumor, thus affecting the effect of MR molecular imaging[57]. It can be optimized from the following aspects: (1) Improve the biocompatibility of molecular probes and appropriately prolong their blood circulation time to promote more molecular probes to bind to the tumor; (2) The molecular probe simultaneously combines more Gd ions to obtain higher relaxation rate[43]; (3) Multi-target molecular imaging facilitates specific imaging of lesions[42]; and (4) Reduce the volume and molecular weight of

molecular probe to achieve better penetration efficiency, paramagnetic resonance effect, reduce immunity and reticuloendothelial system uptake *in vivo*[42].

Different imaging techniques have their advantages and disadvantages, and their combined application can achieve complementary advantages and improve the value of clinical applications[58]. In addition, the management of radiopharmaceuticals is extremely strict in some countries, and very few radiopharmaceuticals are clinically approved. Therefore, in addition to the research and development of various imaging agents with high specificity and high sensitivity mentioned above, AI technology to improve diagnostic performance or complement existing technologies may be worth exploring.

ARTIFICIAL INTELLIGENCE AND RADIOMICS

AI, artificial intelligence, can be used to mine various medical images for biometric information and imaging features that are not easily perceived by physicians. In recent years, the application of AI-based radiomics has been used for lesion detection, pathological diagnosis, radiotherapy target delineation and curative effect prediction, so as to improve effective treatment decision-making for cancer patients. Based on radiomics, the cross-validated support vector machine classification diagnostic model can automatically extract quantitative features from MDCT[59]. Liu *et al*[60] used the AI system of R-CNN depth neural network to verify the diagnosis of CT images of pancreatic carcinoma in 100 cases, and established an AI diagnosis system of pancreatic carcinoma based on enhanced CT images. The system can assist doctors to identify pancreatic carcinoma, normal pancreatic tissue, chronic pancreatitis or benign pancreatic tumors. Mori *et al*[61] constructed ^{18}F-FDG-PET/CT radiomic model to predict the recurrence survival value of patients with LAPC after radiotherapy for locally advanced pancreatic cancer, which could significantly improve treatment outcome while avoiding over-treatment of patients with poorer expected outcomes.

Radiomics based on AI has the potential to supplement information for clinical diagnosis and treatment and help solve certain clinical problems, but there are some limitations, such as incorrect tumor screening, insufficient design of database, case number and sensitive feature algorithm.

CONCLUSION

Nuclear medicine molecular imaging is based on the principle of injecting microscopic molecular probes into the body and selectively targeting them to appropriate sites based on different properties, in order to qualify or quantify organs, tissues or lesions for assessing diseases at the molecular level. Molecular imaging in nuclear medicine has made significant advances in the assessment of pancreatic carcinoma in recent years.

FOOTNOTES

Author contributions: Pang XX and Xie L wrote the paper; Pan B provided cases of 18F-FDG *vs* 18F-FAPI PET/CT scan and advice on 18F-FDG *vs* 18F-FAPI of pancreatic carcinoma; Yao WJ and Liu XX provided advice on MRI scan of pancreatic carcinoma; Chen N and Pang XX cooperated on scientific research in Gd-DOTA-HHK and 99mTc-DOTA-HHK compounds.

Supported by The Basic and Clinical Cooperative Research Promotion Plan of Anhui Medical University, No. 2019xkjT011; Anhui Provincial Natural Science Foundation, No. 2008085QH406; and Anhui Medical University Joint Project of Nuclear Medicine and Radiation Medicine, No. 2021 Lcxk035.

Conflict-of-interest statement: The authors have declared that no conflicts of interest exist.

Country/Territory of origin: China

ORCID number: Xiao-Xi Pang 0000-0002-1303-5224; Liang Xie 0000-0002-3748-0648; Wen-Jun Yao 0000-0002-6504-7673; Bo Pan 0000-0002-9167-6983; Ni Chen 0000-0001-7533-7546.

S-Editor: Wang JL

L-Editor: A
P-Editor: Chen YX

REFERENCES

1 **Siegel RL**, Miller KD, Jemal A. Cancer statistics, 2020. *CA Cancer J Clin* 2020; **70**: 7-30 [PMID: 31912902 DOI: 10.3322/caac.21590]
2 **Sellmyer MA**, Lee IK, Mankoff DA. Building the Bridge: Molecular Imaging Biomarkers for 21(st) Century Cancer Therapies. *J Nucl Med* 2021; **62**: 1672-1676 [PMID: 34446450 DOI: 10.2967/jnumed.121.262484]
3 **Peppicelli S**, Andreucci E, Ruzzolini J, Bianchini F, Calorini L. FDG uptake in cancer: a continuing debate. *Theranostics* 2020; **10**: 2944-2948 [PMID: 32194847 DOI: 10.7150/thno.40599]
4 **Ghaneh P**, Hanson R, Titman A, Lancaster G, Plumpton C, Lloyd-Williams H, Yeo ST, Edwards RT, Johnson C, Abu Hilal M, Higginson AP, Armstrong T, Smith A, Scarsbrook A, McKay C, Carter R, Sutcliffe RP, Bramhall S, Kocher HM, Cunningham D, Pereira SP, Davidson B, Chang D, Khan S, Zealley I, Sarker D, Al Sarireh B, Charnley R, Lobo D, Nicolson M, Halloran C, Raraty M, Sutton R, Vinjamuri S, Evans J, Campbell F, Deeks J, Sanghera B, Wong WL, Neoptolemos JP. PET-PANC: multicentre prospective diagnostic accuracy and health economic analysis study of the impact of combined modality 18fluorine-2-fluoro-2-deoxy-d-glucose positron emission tomography with computed tomography scanning in the diagnosis and management of pancreatic cancer. *Health Technol Assess* 2018; **22**: 1-114 [PMID: 29402376 DOI: 10.3310/hta22070]
5 **Daamen LA**, Groot VP, Goense L, Wessels FJ, Borel Rinkes IH, Intven MPW, van Santvoort HC, Molenaar IQ. The diagnostic performance of CT versus FDG PET-CT for the detection of recurrent pancreatic cancer: a systematic review and meta-analysis. *Eur J Radiol* 2018; **106**: 128-136 [PMID: 30150034 DOI: 10.1016/j.ejrad.2018.07.010]
6 **Topkan E**, Parlak C, Yapar AF. FDG-PET/CT-based restaging may alter initial management decisions and clinical outcomes in patients with locally advanced pancreatic carcinoma planned to undergo chemoradiotherapy. *Cancer Imaging* 2013; **13**: 423-428 [PMID: 24240137 DOI: 10.1102/1470-7330.2013.0035]
7 **Xi Y**, Guo R, Hu J, Zhang M, Zhang X, Li B. ^{18}F-fluoro-2-deoxy-D-glucose retention index as a prognostic parameter in patients with pancreatic cancer. *Nucl Med Commun* 2014; **35**: 1112-1118 [PMID: 25098308 DOI: 10.1097/MNM.0000000000000178]
8 **Ahn SJ**, Park MS, Lee JD, Kang WJ. Correlation between ^{18}F-fluorodeoxyglucose positron emission tomography and pathologic differentiation in pancreatic cancer. *Ann Nucl Med* 2014; **28**: 430-435 [PMID: 24623151 DOI: 10.1007/s12149-014-0833-x]
9 **Myssayev A**, Myssayev A, Ideguchi R, Eguchi S, Adachi T, Sumida Y, Tobinaga S, Uetani M, Kudo T. Usefulness of FDG PET/CT derived parameters in prediction of histopathological finding during the surgery in patients with pancreatic adenocarcinoma. *PLoS One* 2019; **14**: e0210178 [PMID: 30629646 DOI: 10.1371/journal.pone.0210178]
10 **Barreto SG**, Loveday B, Windsor JA, Pandanaboyana S. Detecting tumour response and predicting resectability after neoadjuvant therapy for borderline resectable and locally advanced pancreatic cancer. *ANZ J Surg* 2019; **89**: 481-487 [PMID: 30117669 DOI: 10.1111/ans.14764]
11 **Hyun SH**, Kim HS, Choi SH, Choi DW, Lee JK, Lee KH, Park JO, Kim BT, Choi JY. Intratumoral heterogeneity of (18)F-FDG uptake predicts survival in patients with pancreatic ductal adenocarcinoma. *Eur J Nucl Med Mol Imaging* 2016; **43**: 1461-1468 [PMID: 26872788 DOI: 10.1007/s00259-016-3316-6]
12 **Chang JS**, Choi SH, Lee Y, Kim KH, Park JY, Song SY, Cho A, Yun M, Lee JD, Seong J. Clinical usefulness of ^{18}F-fluorodeoxyglucose-positron emission tomography in patients with locally advanced pancreatic cancer planned to undergo concurrent chemoradiation therapy. *Int J Radiat Oncol Biol Phys* 2014; **90**: 126-133 [PMID: 25015206 DOI: 10.1016/j.ijrobp.2014.05.030]
13 **Moon SY**, Joo KR, So YR, Lim JU, Cha JM, Shin HP, Yang YJ. Predictive value of maximum standardized uptake value (SUVmax) on ^{18}F-FDG PET/CT in patients with locally advanced or metastatic pancreatic cancer. *Clin Nucl Med* 2013; **38**: 778-783 [PMID: 24107806 DOI: 10.1097/RLU.0b013e31829f8c90]
14 **Zhang A**, Ren S, Yuan Y, Li X, Zhu X, Jiang L, Li D, Zuo C. Prognostic values of ^{18}F-FDG PET/CT metabolic parameters and clinical figures in locally advanced pancreatic cancer underwent chemotherapy combined with stereotactic body radiation therapy. *Medicine (Baltimore)* 2019; **98**: e15064 [PMID: 30921238 DOI: 10.1097/MD.0000000000015064]
15 **Yamamoto T**, Sugiura T, Mizuno T, Okamura Y, Aramaki T, Endo M, Uesaka K. Preoperative FDG-PET predicts early recurrence and a poor prognosis after resection of pancreatic adenocarcinoma. *Ann Surg Oncol* 2015; **22**: 677-684 [PMID: 25190125 DOI: 10.1245/s10434-014-4046-2]
16 **Pu Y**, Wang C, Zhao S, Xie R, Zhao L, Li K, Yang C, Zhang R, Tian Y, Tan L, Li J, Li S, Chen L, Sun H. The clinical application of (18)F-FDG PET/CT in pancreatic cancer: a narrative review. *Transl Cancer Res* 2021; **10**: 3560-3575 [PMID: 35116659 DOI: 10.21037/tcr-21-169]
17 **Calabrò D**, Argalia G, Ambrosini V. Role of PET/CT and Therapy Management of Pancreatic Neuroendocrine Tumors. *Diagnostics (Basel)* 2020; **10** [PMID: 33297381 DOI: 10.3390/diagnostics10121059]
18 **Carideo L**, Prosperi D, Panzuto F, Magi L, Pratesi MS, Rinzivillo M, Annibale B, Signore A. Role of Combined [(68)Ga]Ga-DOTA-SST Analogues and [(18)F]FDG PET/CT in the Management of GEP-NENs: A Systematic Review. *J Clin Med* 2019; **8** [PMID: 31337043 DOI: 10.3390/jcm8071032]
19 **Zhang P**, Yu J, Li J, Shen L, Li N, Zhu H, Zhai S, Zhang Y, Yang Z, Lu M. Clinical and Prognostic Value of PET/CT Imaging with Combination of (68)Ga-DOTATATE and (18)F-FDG in Gastroenteropancreatic Neuroendocrine Neoplasms. *Contrast Media Mol Imaging* 2018; **2018**: 2340389 [PMID: 29681780 DOI: 10.1155/2018/2340389]
20 **Evangelista L**, Ravelli I, Bignotto A, Cecchin D, Zucchetta P. Ga-68 DOTA-peptides and F-18 FDG PET/CT in patients with neuroendocrine tumor: A review. *Clin Imaging* 2020; **67**: 113-116 [PMID: 32559681 DOI:

10.1016/j.clinimag.2020.05.035]
21 **Fani M**, Nicolas GP, Wild D. Somatostatin Receptor Antagonists for Imaging and Therapy. *J Nucl Med* 2017; **58**: 61S-66S [PMID: 28864614 DOI: 10.2967/jnumed.116.186783]
22 **Liu Y**, Watabe T, Kaneda-Nakashima K, Shirakami Y, Naka S, Ooe K, Toyoshima A, Nagata K, Haberkorn U, Kratochwil C, Shinohara A, Hatazawa J, Giesel F. Fibroblast activation protein targeted therapy using [(177)Lu]FAPI-46 compared with [(225)Ac]FAPI-46 in a pancreatic cancer model. *Eur J Nucl Med Mol Imaging* 2022; **49**: 871-880 [PMID: 34537893 DOI: 10.1007/s00259-021-05554-2]
23 **Sunami Y**, Häußler J, Kleeff J. Cellular Heterogeneity of Pancreatic Stellate Cells, Mesenchymal Stem Cells, and Cancer-Associated Fibroblasts in Pancreatic Cancer. *Cancers (Basel)* 2020; **12** [PMID: 33333727 DOI: 10.3390/cancers12123770]
24 **Ji X**, Qian J, Rahman SMJ, Siska PJ, Zou Y, Harris BK, Hoeksema MD, Trenary IA, Heidi C, Eisenberg R, Rathmell JC, Young JD, Massion PP. xCT (SLC7A11)-mediated metabolic reprogramming promotes non-small cell lung cancer progression. *Oncogene* 2018; **37**: 5007-5019 [PMID: 29789716 DOI: 10.1038/s41388-018-0307-z]
25 **Zhang L**, Huang Y, Ling J, Zhuo W, Yu Z, Luo Y, Zhu Y. Overexpression of SLC7A11: a novel oncogene and an indicator of unfavorable prognosis for liver carcinoma. *Future Oncol* 2018; **14**: 927-936 [PMID: 29528250 DOI: 10.2217/fon-2017-0540]
26 **Zhang Z**, Jia G, Pan G, Cao K, Yang Q, Meng H, Yang J, Zhang L, Wang T, Cheng C, Zuo C. Comparison of the diagnostic efficacy of (68) Ga-FAPI-04 PET/MR and (18)F-FDG PET/CT in patients with pancreatic cancer. *Eur J Nucl Med Mol Imaging* 2022; **49**: 2877-2888 [PMID: 35243518 DOI: 10.1007/s00259-022-05729-5]
27 **Röhrich M**, Naumann P, Giesel FL, Choyke PL, Staudinger F, Wefers A, Liew DP, Kratochwil C, Rathke H, Liermann J, Herfarth K, Jäger D, Debus J, Haberkorn U, Lang M, Koerber SA. Impact of (68)Ga-FAPI PET/CT Imaging on the Therapeutic Management of Primary and Recurrent Pancreatic Ductal Adenocarcinomas. *J Nucl Med* 2021; **62**: 779-786 [PMID: 33097632 DOI: 10.2967/jnumed.120.253062]
28 **Gallo A**, Dedionigi C, Civitelli C, Panzeri A, Corradi C, Squizzato A. Optimal Management of Cirrhotic Ascites: A Review for Internal Medicine Physicians. *J Transl Int Med* 2020; **8**: 220-236 [PMID: 33511049 DOI: 10.2478/jtim-2020-0035]
29 **Deng M**, Chen Y, Cai L. Comparison of 68Ga-FAPI and ^{18}F-FDG PET/CT in the Imaging of Pancreatic Cancer With Liver Metastases. *Clin Nucl Med* 2021; **46**: 589-591 [PMID: 33630809 DOI: 10.1097/RLU.0000000000003561]
30 **Xiong J**, Balcioglu HE, Danen EH. Integrin signaling in control of tumor growth and progression. *Int J Biochem Cell Biol* 2013; **45**: 1012-1015 [PMID: 23428797 DOI: 10.1016/j.biocel.2013.02.005]
31 **Herter J**, Zarbock A. Integrin Regulation during Leukocyte Recruitment. *J Immunol* 2013; **190**: 4451-4457 [PMID: 23606722 DOI: 10.4049/jimmunol.1203179]
32 **Huo Y**, Kang L, Pang X, Shen H, Yan P, Zhang C, Liao X, Chen X, Wang R. Noninvasive PET Imaging of a Ga-68-Radiolabeled RRL-Derived Peptide in Hepatocarcinoma Murine Models. *Mol Imaging Biol* 2019; **21**: 286-296 [PMID: 29916116 DOI: 10.1007/s11307-018-1234-7]
33 **Reader CS**, Vallath S, Steele CW, Haider S, Brentnall A, Desai A, Moore KM, Jamieson NB, Chang D, Bailey P, Scarpa A, Lawlor R, Chelala C, Keyse SM, Biankin A, Morton JP, Evans TJ, Barry ST, Sansom OJ, Kocher HM, Marshall JF. The integrin αvβ6 drives pancreatic cancer through diverse mechanisms and represents an effective target for therapy. *J Pathol* 2019; **249**: 332-342 [PMID: 31259422 DOI: 10.1002/path.5320]
34 **Liu Z**, Liu H, Ma T, Sun X, Shi J, Jia B, Sun Y, Zhan J, Zhang H, Zhu Z, Wang F. Integrin αvβ$_6$-Targeted SPECT Imaging for Pancreatic Cancer Detection. *J Nucl Med* 2014; **55**: 989-994 [PMID: 24711651 DOI: 10.2967/jnumed.113.132969]
35 **Koay EJ**, Hall W, Park PC, Erickson B, Herman JM. The role of imaging in the clinical practice of radiation oncology for pancreatic cancer. *Abdom Radiol (NY)* 2018; **43**: 393-403 [PMID: 29110053 DOI: 10.1007/s00261-017-1373-3]
36 **Higaki T**, Nakamura Y, Tatsugami F, Kaichi Y, Akagi M, Akiyama Y, Baba Y, Iida M, Awai K. Introduction to the Technical Aspects of Computed Diffusion-weighted Imaging for Radiologists. *Radiographics* 2018; **38**: 1131-1144 [PMID: 29995614 DOI: 10.1148/rg.2018170115]
37 **Liang L**, Gu JY, Liu K, Fu CX, Rao SX, Zeng MS. [Application of cDWI in diagnosis of pancreatic cancer: a preliminary study]. *Fangshexue Shijian* 2019; **34**: 1081-1087 [DOI: 10.13609/j.cnki.1000-0313.2019.10.006]
38 **Kaandorp MPT**, Barbieri S, Klaassen R, van Laarhoven HWM, Crezee H, While PT, Nederveen AJ, Gurney-Champion OJ. Improved unsupervised physics-informed deep learning for intravoxel incoherent motion modeling and evaluation in pancreatic cancer patients. *Magn Reson Med* 2021; **86**: 2250-2265 [PMID: 34105184 DOI: 10.1002/mrm.28852]
39 **Ottens T**, Barbieri S, Orton MR, Klaassen R, van Laarhoven HWM, Crezee H, Nederveen AJ, Zhen X, Gurney-Champion OJ. Deep learning DCE-MRI parameter estimation: Application in pancreatic cancer. *Med Image Anal* 2022; **80**: 102512 [PMID: 35709559 DOI: 10.1016/j.media.2022.102512]
40 **Valenzuela RF**, Kundra V, Madewell JE, Costelloe CM. Advanced Imaging in Musculoskeletal Oncology: Moving Away From RECIST and Embracing Advanced Bone and Soft Tissue Tumor Imaging (ABASTI) - Part I - Tumor Response Criteria and Established Functional Imaging Techniques. *Semin Ultrasound CT MR* 2021; **42**: 201-214 [PMID: 33814106 DOI: 10.1053/j.sult.2020.08.012]
41 **Chen X**, Zhou H, Li X, Duan N, Hu S, Liu Y, Yue Y, Song L, Zhang Y, Li D, Wang Z. Plectin-1 Targeted Dual-modality Nanoparticles for Pancreatic Cancer Imaging. *EBioMedicine* 2018; **30**: 129-137 [PMID: 29574092 DOI: 10.1016/j.ebiom.2018.03.008]
42 **Wang Q**, Yan H, Jin Y, Wang Z, Huang W, Qiu J, Kang F, Wang K, Zhao X, Tian J. A novel plectin/integrin-targeted bispecific molecular probe for magnetic resonance/near-infrared imaging of pancreatic cancer. *Biomaterials* 2018; **183**: 173-184 [PMID: 30172243 DOI: 10.1016/j.biomaterials.2018.08.048]
43 **Huang X**, Fan C, Zhu H, Le W, Cui S, Chen X, Li W, Zhang F, Huang Y, Sh D, Cui Z, Shao C, Chen B. Glypican-1-antibody-conjugated Gd-Au nanoclusters for FI/MRI dual-modal targeted detection of pancreatic cancer. *Int J Nanomedicine* 2018; **13**: 2585-2599 [PMID: 29750031 DOI: 10.2147/IJN.S158559]
44 **Lee S**, Kim SH, Park HK, Jang KT, Hwang JA, Kim S. Pancreatic Ductal Adenocarcinoma: Rim Enhancement at MR Imaging Predicts Prognosis after Curative Resection. *Radiology* 2018; **288**: 456-466 [PMID: 29664340 DOI: 10.1148/radiol.2018172331]
45 **Zhang C**, Yan Y, Zou Q, Chen J, Li C. Superparamagnetic iron oxide nanoparticles for MR imaging of pancreatic cancer:

Potential for early diagnosis through targeted strategies. *Asia Pac J Clin Oncol* 2016; **12**: 13-21 [PMID: 26663873 DOI: 10.1111/ajco.12437]

46 **Ze X**, Zou W, Li Z. Translational research in anti-pancreatic fibrosis drug discovery and development. *J Transl Int Med* 2021; **9**: 225-227 [PMID: 35136719 DOI: 10.2478/jtim-2021-0036]

47 **Ahmadi Y**, Kostenich G, Oron-Herman M, Wadsak W, Mitterhauser M, Orenstein A, Mirzaei S, Knoll P. In vivo magnetic resonance imaging of pancreatic tumors using iron oxide nanoworms targeted with PTR86 peptide. *Colloids Surf B Biointerfaces* 2017; **158**: 423-430 [PMID: 28719864 DOI: 10.1016/j.colsurfb.2017.06.051]

48 **Li H**, Wang P, Gong W, Wang Q, Zhou J, Zhu WH, Cheng Y. Dendron-Grafted Polylysine-Based Dual-Modal Nanoprobe for Ultra-Early Diagnosis of Pancreatic Precancerosis *via* Targeting a Urokinase-Type Plasminogen Activator Receptor. *Adv Healthc Mater* 2018; **7** [PMID: 29195018 DOI: 10.1002/adhm.201700912]

49 **Morin E**, Sjöberg E, Tjomsland V, Testini C, Lindskog C, Franklin O, Sund M, Öhlund D, Kiflemariam S, Sjöblom T, Claesson-Welsh L. VEGF receptor-2/neuropilin 1 trans-complex formation between endothelial and tumor cells is an independent predictor of pancreatic cancer survival. *J Pathol* 2018; **246**: 311-322 [PMID: 30027561 DOI: 10.1002/path.5141]

50 **Zhang W**, Liang X, Zhu L, Zhang X, Jin Z, Du Y, Tian J, Xue H. Optical magnetic multimodality imaging of plectin-1-targeted imaging agent for the precise detection of orthotopic pancreatic ductal adenocarcinoma in mice. *EBioMedicine* 2022; **80**: 104040 [PMID: 35525203 DOI: 10.1016/j.ebiom.2022.104040]

51 **Zou Q**, Zhang CJ, Yan YZ, Min ZJ, Li CS. MUC-1 aptamer targeted superparamagnetic iron oxide nanoparticles for magnetic resonance imaging of pancreatic cancer in vivo and in vitro experiment. *J Cell Biochem* 2019; **120**: 18650-18658 [PMID: 31338877 DOI: 10.1002/jcb.28950]

52 **Zou J**, Chen S, Li Y, Zeng L, Lian G, Li J, Huang K, Chen Y. Nanoparticles modified by triple single chain antibodies for MRI examination and targeted therapy in pancreatic cancer. *Nanoscale* 2020; **12**: 4473-4490 [PMID: 32031201 DOI: 10.1039/c9nr04976b]

53 **Ramsay EE**, Decollogne S, Joshi S, Corti A, Apte M, Pompella A, Hogg PJ, Dilda PJ. Employing pancreatic tumor γ-glutamyltransferase for therapeutic delivery. *Mol Pharm* 2014; **11**: 1500-1511 [PMID: 24654974 DOI: 10.1021/mp400664t]

54 **Jiang Y**, Liu S, Zhang Y, Li H, He H, Dai J, Jiang T, Ji W, Geng D, Elzatahry AA, Alghamdi A, Fu D, Deng Y, Zhao D. Magnetic mesoporous nanospheres anchored with LyP-1 as an efficient pancreatic cancer probe. *Biomaterials* 2017; **115**: 9-18 [PMID: 27871003 DOI: 10.1016/j.biomaterials.2016.11.006]

55 **Nahm CB**, Turchini J, Jamieson N, Moon E, Sioson L, Itchins M, Arena J, Colvin E, Howell VM, Pavlakis N, Clarke S, Samra JS, Gill AJ, Mittal A. Biomarker panel predicts survival after resection in pancreatic ductal adenocarcinoma: A multi-institutional cohort study. *Eur J Surg Oncol* 2019; **45**: 218-224 [PMID: 30348604 DOI: 10.1016/j.ejso.2018.10.050]

56 **Tummers WS**, Willmann JK, Bonsing BA, Vahrmeijer AL, Gambhir SS, Swijnenburg RJ. Advances in Diagnostic and Intraoperative Molecular Imaging of Pancreatic Cancer. *Pancreas* 2018; **47**: 675-689 [PMID: 29894417 DOI: 10.1097/MPA.0000000000001075]

57 **Dadfar SM**, Roemhild K, Drude NI, von Stillfried S, Knüchel R, Kiessling F, Lammers T. Iron oxide nanoparticles: Diagnostic, therapeutic and theranostic applications. *Adv Drug Deliv Rev* 2019; **138**: 302-325 [PMID: 30639256 DOI: 10.1016/j.addr.2019.01.005]

58 **Feng L**, Guo J, Wang S, Liu X, Ge N, Wang G, Sun S. Endoscopic Transmural Drainage and Necrosectomy in Acute Necrotizing Pancreatitis: A Review. *J Transl Int Med* 2021; **9**: 168-176 [PMID: 34900627 DOI: 10.2478/jtim-2021-0031]

59 **Wei R**, Lin K, Yan W, Guo Y, Wang Y, Li J, Zhu J. Computer-Aided Diagnosis of Pancreas Serous Cystic Neoplasms: A Radiomics Method on Preoperative MDCT Images. *Technol Cancer Res Treat* 2019; **18**: 1533033818824339 [PMID: 30803366 DOI: 10.1177/1533033818824339]

60 **Liu SL**, Li S, Guo YT, Zhou YP, Zhang ZD, Lu Y. Establishment and application of an artificial intelligence diagnosis system for pancreatic cancer with a faster region-based convolutional neural network. *Chin Med J (Engl)* 2019; **132**: 2795-2803 [PMID: 31856050 DOI: 10.1097/CM9.0000000000000544]

61 **Mori M**, Passoni P, Incerti E, Bettinardi V, Broggi S, Reni M, Whybra P, Spezi E, Vanoli EG, Gianolli L, Picchio M, Di Muzio NG, Fiorino C. Training and validation of a robust PET radiomic-based index to predict distant-relapse-free-survival after radio-chemotherapy for locally advanced pancreatic cancer. *Radiother Oncol* 2020; **153**: 258-264 [PMID: 32681930 DOI: 10.1016/j.radonc.2020.07.003]

World Journal of Radiology

Submit a Manuscript: https://www.f6publishing.com

World J Radiol 2023 January 28; 15(1): 20-31

DOI: 10.4329/wjr.v15.i1.20

ISSN 1949-8470 (online)

ORIGINAL ARTICLE

Retrospective Study

Diagnostic efficacy of diffusion-weighted imaging and semiquantitative and quantitative dynamic contrast-enhanced magnetic resonance imaging in salivary gland tumors

Erkan Gökçe, Murat Beyhan

Specialty type: Radiology, nuclear medicine and medical imaging

Provenance and peer review: Invited article; Externally peer reviewed.

Peer-review model: Single blind

Peer-review report's scientific quality classification

Grade A (Excellent): 0
Grade B (Very good): B
Grade C (Good): C
Grade D (Fair): 0
Grade E (Poor): 0

P-Reviewer: Li T, China; Ma C, China

Received: July 5, 2022
Peer-review started: July 5, 2022
First decision: September 5, 2022
Revised: September 15, 2022
Accepted: December 13, 2022
Article in press: December 13, 2022
Published online: January 28, 2023

Erkan Gökçe, Murat Beyhan, Department of Radiology, Tokat Gaziosmanpasa University, Faculty of Medicine, Tokat 60100, Turkey

Corresponding author: Erkan Gökçe, MD, Professor, Department of Radiology, Tokat Gaziosmanpasa University, Faculty of Medicine, Kaleardı Neighborhood, Muhittin Fisunoglu Street, Tokat 60100, Turkey. drerkangokce@gmail.com

Abstract

BACKGROUND

Increased use of functional magnetic resonance imaging (MRI) methods such as diffusion-weighted imaging (DWI) and dynamic contrast-enhanced (DCE) MRI consisting of sequential contrast series, allows us to obtain more information on the microstructure, cellularity, interstitial distance, and vascularity of tumors, which has increased the discrimination power for benign and malignant salivary gland tumors (SGTs). In the last few years, quantitative DCE MRI data containing T1 perfusion parameters (K_{trans}, K_{ep} and V_e), were reported to contribute to the differentiation of benign or malignant subtypes in SGTs.

AIM

To evaluate the diagnostic efficacy of DWI and semiquantitative and quantitative perfusion MRI parameters in SGTs.

METHODS

Diffusion MRI [apparent diffusion coefficient (ADC) value] with a 1.5 T MR machine, semiquantitative perfusion MRI [time intensity curve (TIC) pattern], and quantitative perfusion MRI examinations (K_{trans}, K_{ep} and V_e) of 73 tumors in 67 patients with histopathological diagnosis performed from 2017 to 2021 were retrospectively evaluated. In the ADC value and semiquantitative perfusion MRI measurements, cystic components of the tumors were not considered, and the region of interest (ROI) was manually placed through the widest axial section of the tumor. TIC patterns were divided into four groups: Type A = T_{peak} > 120 s; type B = T_{peak} ≤ 120 s, washout ratio (WR) ≥ 30%; type C = T_{peak} ≤ 120 s, WR < 30%; and type D = flat TIC. For the quantitative perfusion MRI analysis, a 3D ROI was placed in the largest solid component of the tumor, and the K_{trans}, K_{ep} and V_e values were automatically generated.

RESULTS

The majority of SGTs were located in the parotid glands (86.3%). Of all the SGTs, 68.5% were benign and 31.5% were malignant. Significant differences were found for ADC values among pleomorphic adenomas (PMAs), Warthin's tumors (WTs), and malignant tumors (MTs) ($P < 0.001$). PMAs had type A and WTs had type B TIC pattern while the vast majority of MTs and other benign tumors (OBTs) (54.5% and 45.5%, respectively) displayed type C TIC pattern. PMAs showed no washout, while the highest mean WR was observed in WTs (59% ± 11%). K_{trans} values of PMAs, WTs, OBTs, and MTs were not significantly different. K_{ep} values of PMAs and WTs were significantly different from those of OBTs and MTs. Mean V_e value of WTs was significantly different from those of PMAs, OBTs, and MTs ($P < 0.001$).

CONCLUSION

The use of quantitative DCE parameters along with diffusion MRI and semiquantitative contrast-enhanced MRI in SGTs could improve the diagnostic accuracy.

Key Words: Diffusion-weighted imaging; Dynamic contrast-enhanced imaging; Magnetic resonance imaging; Perfusion imaging; Salivary gland tumor; Tumor

Core Tip: In this study, the diagnostic features of diffusion-weighted imaging and semiquantitative and quantitative perfusion magnetic resonance imaging (MRI) parameters were evaluated in salivary gland tumors. The apparent diffusion coefficient (ADC) values of pleomorphic adenomas (PMAs) were significantly higher than those of Warthin's tumors (WTs), other benign tumors (OBTs), and malignant tumors (MTs). On semiquantitative MRI, PMAs were distinguished from all other tumors by their long T_{peak} times and lack of washout. WTs had the shortest T_{peak} and highest washout ratio values. For quantitative perfusion MRI parameters, the K_{ep} value of WTs was significantly higher than those of other tumors. The V_e values of WTs and OBTs differed significantly from those of PMAs and MTs.

Citation: Gökçe E, Beyhan M. Diagnostic efficacy of diffusion-weighted imaging and semiquantitative and quantitative dynamic contrast-enhanced magnetic resonance imaging in salivary gland tumors. *World J Radiol* 2023; 15(1): 20-31

URL: https://www.wjgnet.com/1949-8470/full/v15/i1/20.htm

DOI: https://dx.doi.org/10.4329/wjr.v15.i1.20

INTRODUCTION

Salivary gland tumors (SGTs) account for about 2.0%-6.5% of all head and neck tumors. Approximately 70% of them originate from the parotid glands, and a small number have submandibular, sublingual, and minor salivary gland origins. While the majority of tumors from the parotid glands are benign, malignancies are more common in those located in other glands. Preoperative characterization of SGTs is important for treatment planning. The choice of surgery method for SGTs is closely associated with the histology of the tumor. Diagnosis is mostly based on combined evaluation of clinical features and findings from physical examinations, imaging and cytological observations. Fine-needle aspiration biopsy (FNAB) is the most commonly used method for cytological examinations but complex pathologies can result in false positives and false negatives in malignant tumors (MTs)[1,2]. Conventional magnetic resonance imaging (MRI) is very useful for identifying the tumor location, morphology, extension, and its association with the nerves and inner structure[1-3]. However, diagnosing MTs and benign tumors (BTs) by conventional MRI can be difficult due to overlapping findings[1,2,4]. In recent years, an increase has been reported in diagnostic accuracy in SGTs for distinguishing between MTs and BTs with the use of diffusion-weighted imaging (DWI) and dynamic contrast-enhanced (DCE) MRI techniques[1,5-9]. DCE MRI is used to track an exogenous, paramagnetic contrast agent in tissues and has been a powerful tool in the characterization of tumor hemodynamics[1,3,10,11]. As a semiquantitative method in DCE MRI, patterns have been established by measuring time to peak (T_{peak}) and washout ratio (WR) on the time intensity curve (TIC)[1,3]. T_{peak} is closely related to microvessel count while WR reflects the stromal cellularity grade. On quantitative DCE MRI, on the other hand, perfusion parameters such as K_{trans} [volume transfer constant between blood plasma and the extracellular extravascular space (EES)], K_{ep} (flux rate constant between the EES and plasma), and V_e (EES fractional volume) are used[1,3]. Although there are many studies dealing with diffusion and semiquantitative

DCE MRIs in SGTs, the number of quantitative MRI studies is limited[12-15]. In the present study, the diagnostic value of diffusion MRI and semiquantitative and quantitative perfusion MRI parameters was evaluated in SGTs.

MATERIALS AND METHODS

Patients

The study was conducted retrospectively following approval by the local ethics committee (20-KAEK-105). A total of 67 patients with tumors originating from or involving the salivary glands were included. The study included patients who had swelling of the face or in the salivary glands, who were subjected to MRI, diffusion MRI, and perfusion MRI examinations at our hospital between April 2017 and February 2021 and who were diagnosed histopathologically after FNAB, Tru-cut biopsy, or surgical removal. For this study, patients whose neck and maxillofacial MRI examination reports included the description of a mass in the salivary glands were surveyed in picture archiving and communication systems. A total of 33 patients were excluded: 2 patients with intra-lesion hemorrhage due to FNAB before the MRI examination, 16 patients who had contrast-enhanced MRI but did not have perfusion MRI series, and 15 patients whose diagnosis was not confirmed histopathologically. Thus, a total of 73 MTs and BTs, which originated from major and minor salivary glands in 67 patients, were included in the study (Figure 1).

MRI scanning and measurements

MRI was performed on a 1.5 T superconducting MRI system [General Electric (GE) Signa Explorer Software Version 25; GE Healthcare, Milwaukee, WI, United States, 2016] with head and neck array coils. Routine MRI sequences included axial T1-weighted [time to repetition/time to echo (TR/TE), 456 ms/8.1 ms], in phase axial T2-weighted (TR/TE, 3711 ms/82.8 ms), sagittal T2-weighted (TR/TE, 4499 ms/88.2 ms), and coronal T2-weighted (TR/TE, 4380 ms/84.6 ms). DCE MRI was performed with a T1-weighted 3D fast spoiled gradient echo sequence [TR/TE/time to inversion, 3.8 ms/1.3 ms/15 ms; flip angle, 20°]. The contrast agent Gd-DTPA (Dotarem, Guerbet, France) was injected after the fourth dynamic sequence acquisition at a rate of 2.0 mL/s *via* the right antecubital vein. The contrast agent was administered at a dose of 0.2 mmoL/kg body weight. Immediately after the injection of the contrast agent, a 20 mL saline flush was carried out at the same injection rate. In total, 18-21 dynamic sequence acquisitions with 30 dynamic images per sequence were performed with total scanning time ranging from 3 min and 11 s to 5 min and 24 s. The location, morphology, and internal structure of the tumor were evaluated by conventional MRI (Figures 2A and B, 3A and B, 4A and B, 5A and B).

DWI was performed using a multislice echo-planar single-shot spin-echo sequence, on the axial plane (TR/TE = 5476 ms/95.4 ms, field of view = 26 cm, matrix = 96 × 128, section thickness = 4-5 mm, and interslice gap = 4 mm). Three diffusion gradients were applied sequentially in the x, y, and z directions with *b* values of 0 and 1000 s/mm^2 (Figure 2B). The acquisition time varied from 60 s to 120 s. The apparent diffusion coefficient (ADC) maps were generated automatically.

"GE Advantage Windows Workstation 4.7" was used to determine ADC values on diffusion MRI and to perform measurements in semiquantitative and quantitative perfusion MRI. Image analysis and region of interest (ROI) measurements were carried out on a consensus basis by two neuroradiologists (Erkan Gökçe and Murat Beyhan with more than 12 and 7 years of work experience, respectively) who were not aware of the clinical status of the patients. On ADC value measurements, cystic components of the tumors were not considered, the ROI was manually placed through the widest axial section of the tumor, and the ADC value was determined as mm^2/s (Figures 2C, 3C, 4C and 5C). Semiquantitative analysis of DCE MRI was based on TIC (Figures 2D and E, 3D and E, 4D and E, 5D and E). T_{peak} was measured as the time from the point where the lesion began to show contrast enhancement to the point with the highest level of contrast enhancement. TICs were evaluated in four different categories based on Yabuuchi *et al*[10]: Type A = T_{peak} > 120 s; type B = T_{peak} ≤ 120 s, WR ≥ 30%; type C = T_{peak} ≤ 120 s, WR < 30%; and type D = flat TIC. To confirm the accuracy of TIC and perfusion biomarker analyses, ROIs were drawn in a way to avoid the vascular and cystic parts of the tumors. Quantitative perfusion DCE MRI parameters were measured using the Tofts kinetic model[16]. For quantitative perfusion MRI analysis, a 3D ROI was placed in the largest solid component of the tumor, and the K_{trans}, K_{ep} and V_e values were generated automatically(Figures 2F-H, 3F-H, 4F-H, 5F-H).

Statistical analysis

Statistical analyses were performed using SPSS 18.0 software (IBM, Chicago, IL, United States) and MedCalc statistical software version 20.009 (MedCalc software bvba, Ostend, Belgium). For each parameter, the conformity of the groups to the normal distribution was evaluated by the Shapiro-Wilk test, and the Levene test was used to evaluate the homogeneity of variances. Data are expressed as the mean ± SD or frequency and percent. One-way ANOVA was used for the groups with a normal distribution for comparison of the groups, and Bonferroni correction was applied in multiple comparisons. The Kruskal-Wallis test was used to compare the groups that did not fit the normal distribution, and

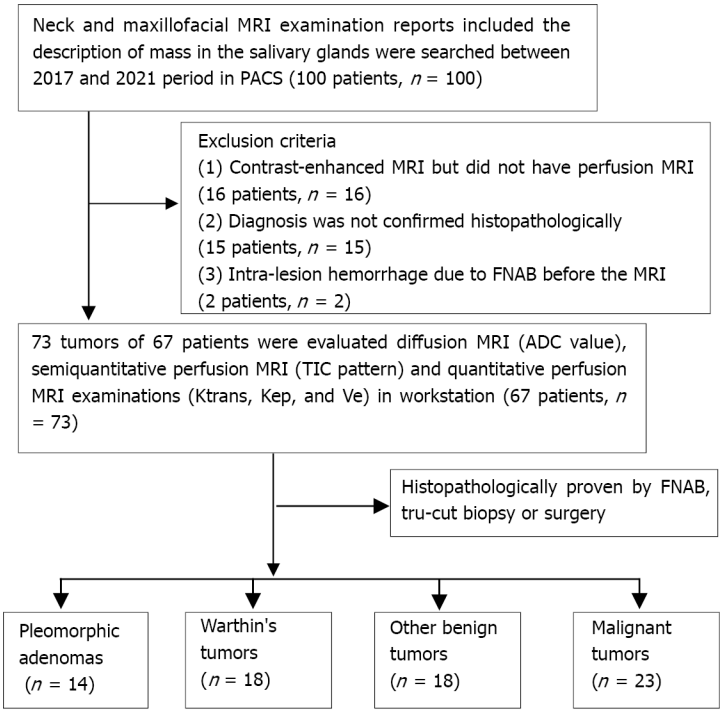

DOI: 10.4329/wjr.v15.i1.20 **Copyright** ©The Author(s) 2023.

Figure 1 Patient inclusion and exclusion flowchart.

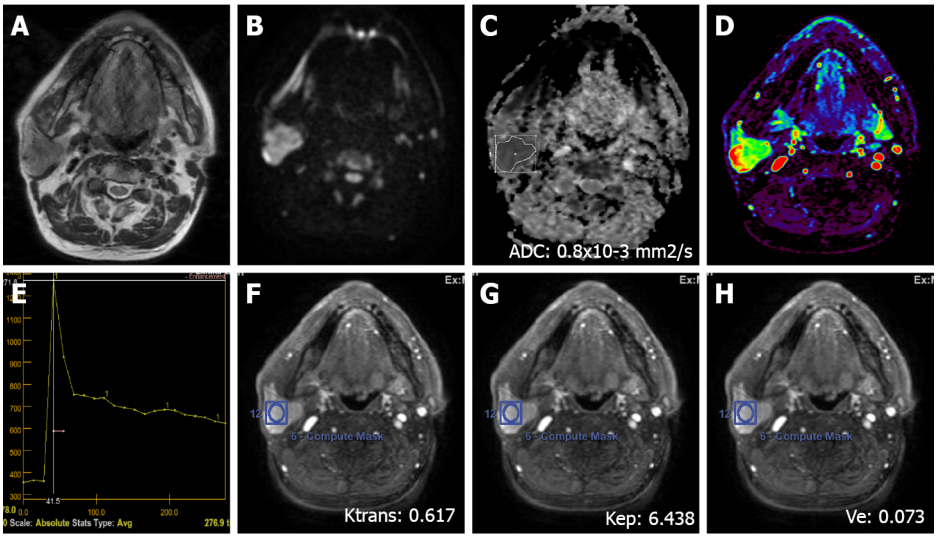

DOI: 10.4329/wjr.v15.i1.20 **Copyright** ©The Author(s) 2023.

Figure 2 A 72-year-old male patient with a Warthin's tumor in the right parotid gland. A: On axial plane T2-weighted image, a mildly hypointense (compared to the gland), smooth-contoured mass localized in the center of the parotid gland is observed; B: On the diffusion-weighted image, the mass appears to be hyperintense; C: ADC value was 0.8 × 10^{-3} mm^2/s on the apparent diffusion coefficient map; D: The mass is hyperperfused on color-coded perfusion image; E: Type B time intensity curve shows a washout ratio of 75%; F, G, and H: K_{trans}, K_{ep}, and V_e values on quantitative perfusion images were 0.617 min^{-1}, 6.438 min^{-1}, and 0.073, respectively. ADC: Apparent diffusion coefficient.

Bonferroni correction was applied in multiple comparisons. The area under curve (AUC), sensitivity, specificity, positive predictive value (PPV), negative predictive value (NPV), and cut-off values of diagnostic parameters were calculated for each tumor group by performing receiver operating characteristic curve (ROC) analysis.

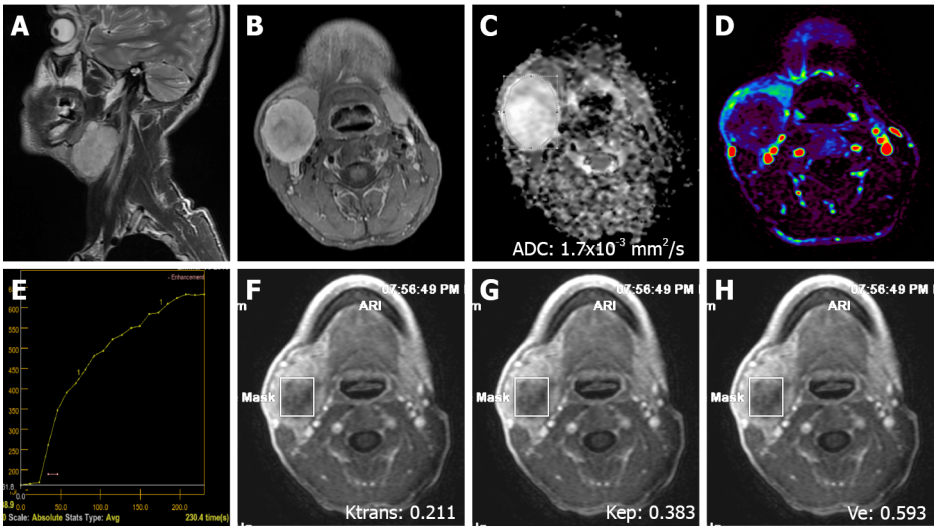

DOI: 10.4329/wjr.v15.i1.20 **Copyright** ©The Author(s) 2023.

Figure 3 A 38-year-old male patient with a pleomorphic adenoma in the right submandibular gland. A: On sagittal plane T2-weighted image, a hyperintense (compared to the gland), smooth, slightly lobule-contoured mass is observed; B: On contrast-enhanced axial plane T1-weighted image, intense contrast-enhancement is observed in the mass; C: The mass is hyperintense on the apparent diffusion coefficient map due to facilitated diffusion (ADC value: 1.7 × 10^{-3} mm^2/s); D: The mass is hypoperfused on color coded perfusion image; E: The tumor has type A time intensity curve; F, G, and H: K_{trans}, K_{ep}, and V_e values on quantitative perfusion images were 0.211 min^{-1}, 0.383 min^{-1}, and 0.593, respectively. ADC: Apparent diffusion coefficient.

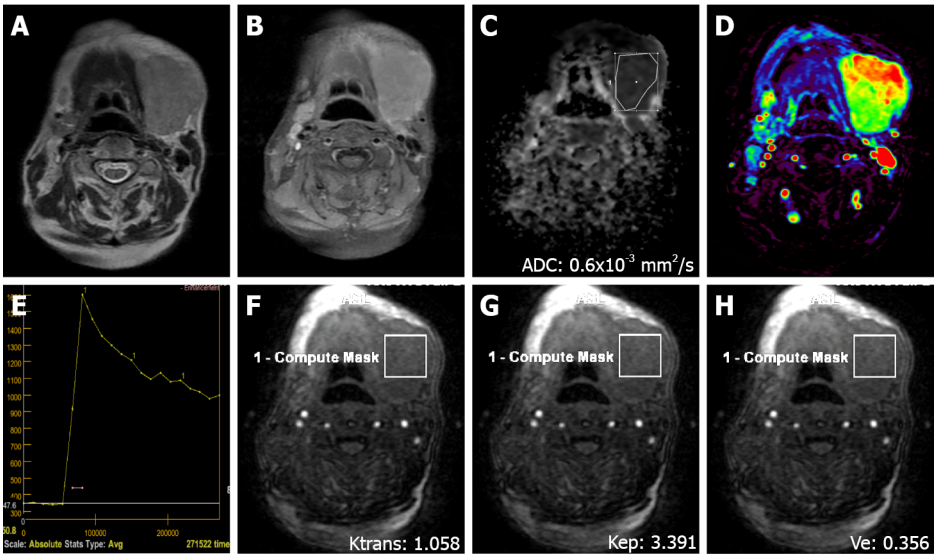

DOI: 10.4329/wjr.v15.i1.20 **Copyright** ©The Author(s) 2023.

Figure 4 A 76-year-old female patient with diffuse large B cell lymphoma and a mass in the left submandibular gland region. A: On axial T2-weighted image, a smooth-contoured mass with homogeneous internal structure and an intensity similar to that of the submandibular gland is observed; B: Axial contrast-enhanced image shows the intense homogeneous contrast enhancement of the mass; C: On the apparent coefficient mapping image, the mass features prominent diffusion restriction (ADC value: 0.6 × 10^{-3} mm^2/s); D: The mass is hyperperfused on color coded perfusion image; E: Type B time intensity curve shows a 48% washout ratio; F, G, and H: K_{trans}, K_{ep}, and V_e values on quantitative perfusion images were 1.058 min^{-1}, 3.391 min^{-1}, and 0.356, respectively. ADC: Apparent diffusion coefficient.

RESULTS

The age range of the 67 patients (40 male and 27 female) included in the study was 12-93 years (mean age = 56.9 ± 15.8 years). One patient had three lesions in the salivary glands, while four patients had two and the remaining 62 had one lesion. Thus, 73 lesions in 67 patients were evaluated. The majority of the lesions (86.3%) were located in the parotid glands, while a small number (4.1%) originated from minor salivary glands. The locations, numbers, and frequencies of SGTs are shown in Table 1. Approximately two-thirds of the lesions (68.5%) were benign (Figures 2 and 3), and one-third (31.5%) was malignant (Figures 4 and 5). Warthin's tumors (WTs) (36.0%) were the most common BTs, followed by pleomorphic adenomas (PMAs) (28.0%). Of the MTs, squamous cell cancer (47.8%), adenoid cystic

Table 1 Locations, numbers, and frequencies of salivary gland tumors

Location	*n* (%)
Unilateral parotid gland	61 (83.6)
Submandibular gland	6 (8.2)
Minor salivary gland	3 (4.1)
Bilateral parotid gland	2 (2.7)
Sublingual gland	1 (1.4)

n: Number of salivary gland tumors

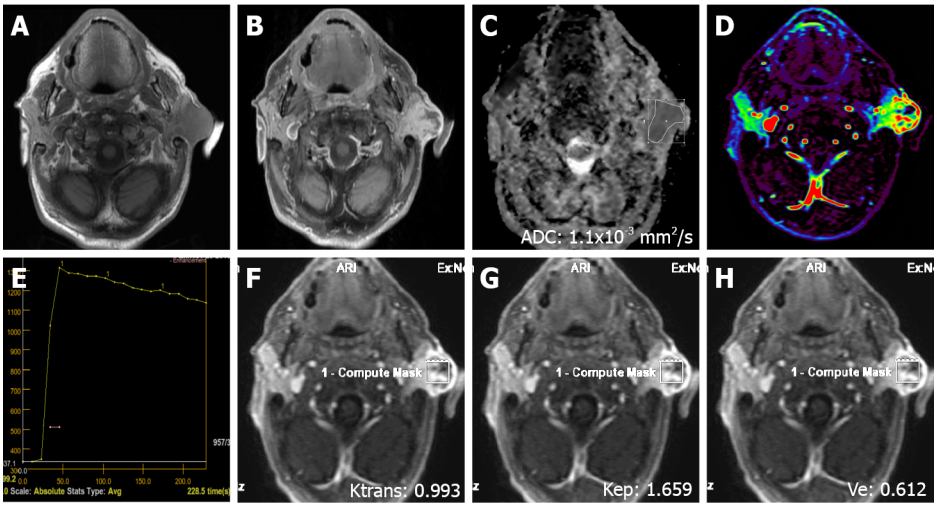

DOI: 10.4329/wjr.v15.i1.20 **Copyright** ©The Author(s) 2023.

Figure 5 A 79-year-old male patient with squamous cell cancer in the left parotid gland. A: On axial plane T1-weighted image, an irregularly contoured, hypointense mass involving skin and subcutaneous tissues is observed; B: On axial contrast-enhanced T1-weighted image, the mass shows an intense heterogeneous contrast enhancement; C: ADC value on the apparent diffusion coefficient map was 1.1 × 10^{-3} mm^2/s; D: The mass is heterogeneously hyperperfused on color coded perfusion image; E: Type C time intensity curve shows a 10% washout ratio; F, G, and H: K_{trans}, K_{ep}, and V_e values on quantitative perfusion images were 0.993 min^{-1}, 1.659 min^{-1}, and 0.612, respectively. ADC: Apparent diffusion coefficient.

cancers (13.0%), and malignant lymphomas (13.0%) were the most common. The numbers of benign and malignant SGTs are provided in Table 2. The ADC values of PMAs were significantly higher than those of WTs, other benign tumors (OBTs), and MTs ($P < 0.001$). However, there was no significant difference in ADC values for OBTs, WTs, and MTs. Significant differences were not found for ADC values of all BTs and MTs. The mean ADC values of SGTs are shown in Table 3.

An evaluation of T_{peak} values of semiquantitative perfusion MRI parameters revealed that PMAs reached T_{peak} significantly later (mean T_{peak} = 202.74 ± 21.48 s) than WTs, OBTs, and MTs while the difference between OBTs and MTs for T_{peak} values was not significant. WTs reached T_{peak} significantly earlier than other tumors. With regard to WR, no washout was observed in PMAs. WTs had the highest mean WR value (59% ± 11%), which was significantly different from the mean WR values of MTs and OBTs. PMAs had type A and WTs had type B TIC pattern, while the majority of MTs and OBTs (54.5% and 45.5%, respectively) exhibited type C TIC pattern. Semiquantitative DCE MRI parameters of SGTs are provided in Table 4.

For quantitative perfusion MRI parameters, K_{trans} values of PMAs, WTs, OBTs, and MTs were not significantly different. The K_{ep} value of WTs, on the other hand, was significantly higher than those of other tumors ($P < 0.001$). For V_e value, WTs and OBTs differed significantly from PMAs and MTs ($P < 0.001$). An evaluation of all BTs and MTs showed significant differences for K_{ep} and V_e values ($P < 0.05$) but not for K_{trans} values. Quantitative DCE MRI parameters of SGTs are shown in Table 3.

The results of ROC analysis and cut-off values used for the parameters of DWI, semiquantitative and quantitative MRI of PMAs, WTs, and malignant SGTs are given in Table 5.

Table 2 Numbers of benign and malignant salivary gland tumors

Benign SGTs	*n* (%)	Malignant SGTs	*n* (%)
Warthin's tumor	18 (24.7)	Squamous cell carcinoma	11 (15.1)
Pleomorphic adenoma	14 (19.2)	Adenoid cystic carcinoma	3 (4.1)
Inflammatory process	12 (16.4)	Malignant lymphoma	3 (4.1)
Lipoma	4 (5.5)	Adenocarcinoma	1 (1.4)
Benign cystic lesions	1 (1.4)	Mucoepidermoid carcinoma	1 (1.4)
		Carcinoma ex pleomorphic adenoma	1 (1.4)
Other benign lesions	1 (1.4)	Acinic cell carcinoma	1 (1.4)
		Follicular dendritic cell sarcoma	1 (1.4)
		Salivary duct carcinoma	1 (1.4)
Total	50 (68.5)		23 (31.5)

SGTs: Salivary gland tumors; *n*: Number of salivary gland tumors

Table 3 Mean ADC values and quantitative dynamic contrast-enhanced magnetic resonance imaging parameters of different histopathologic salivary gland tumors

	Pleomorphic adenoma	Warthin's tumor	Other benign tumors	Malignant tumors	*P* value
ADC ($\times 10^{-3}$ mm^2/s)	1.61 ± 0.26 (a)	0.72 ± 0.09 (b)	0.77 ± 0.19 (b)	0.96 ± 0.33 (b)	< 0.001
K_{trans} (min^{-1})	0.42 ± 0.35	0.75 ± 0.55	0.57 ± 0.37	0.77 ± 0.56	0.131
K_{ep} (min^{-1})	0.69 ± 0.33 (a)	6.2 ± 3.13 (b)	1.95 ± 0.94 (c)	1.72 ± 0.92 (c)	< 0.001
V_e	0.65 ± 0.25 (a)	0.11 ± 0.04 (b)	0.3 ± 0.12 (c)	0.48 ± 0.24 (ac)	< 0.001

Data are shown as the mean ± SD. One-way ANOVA was used. abc: Indicates that means with the same letters in the same column are not significantly different; $P < 0.05$ indicates a statistically significant difference among the groups. ADC: Apparent diffusion coefficient; K_{trans}: Volume transfer constant between blood plasma and the extracellular extravascular space; K_{ep}: Flux rate constant between the EES and plasma; V_e: EES fractional volume; EES: Extracellular extravascular space.

Table 4 Semiquantitative dynamic contrast-enhanced magnetic resonance imaging parameters of different histopathologic salivary gland tumors

	TIC Pattern, *n*(%)				T_{peak} (s)	WR (%)
	A	B	C	D		
Pleomorphic adenomas	14 (70.0)	0 (0)	0 (0)	0 (0)	202.74 ± 21.48 (a)	-
Warthin's tumors	0 (0)	18 (66.7)	0 (0)	0 (0)	20.26 ± 11.72 (b)	59.33 ± 10.99 (a)
Other benign tumors	4 (20.0)	4 (14.8)	10 (45.5)	0 (0)	74.94 ± 75.47 (c)	17.89 ± 14.99 (b)
Malignant tumors	2 (10.0)	5 (18.5)	12 (54.5)	4 (100)	60.60 ± 55.78 (c)	18.48 ± 18.38 (b)
P value	< 0.001				< 0.001	< 0.001

Data are shown as the mean ± SD. One-way ANOVA was used. abc: Indicates that the means with the same letters in the same column are not significantly different. TIC: Time intensity curve; T_{peak}: Time to peak; WR: Washout ratio; *n*: Number of salivary gland tumors.

DISCUSSION

In recent years, diffusion MRI has been an essential complement to conventional sequences in the radiological evaluation of SGTs[1,3,6-10,13-15,17,18]. Diffusion MRI allows us to evaluate the cellularity in tissues and the changes that physiological processes create on microstructural features. As malignant or benign SGTs include a highly heterogeneous group, their ADC values could also be highly variable. In cell-rich tumors such as WT and lymphoma, ADC values are low, but tumors containing hetero-

Table 5 Comparison of pleomorphic adenomas, Warthin's tumors, and malignant salivary gland tumors by ROC analysis using ADC, T_{peak}, K_{trans}, K_{ep}, and V_e values

Variable	Cut-off	AUC (95% CI)	Sensitivity	Specificity	PPV	NPV	*P* value
Pleomorphic adenomas							
ADC value	> 1.1	0.977 (0.911-0.998)	1.000	0.898	0.700	1.000	< 0.001
T_{peak}	> 120	0.947 (0.868-0.986)	1.000	0.898	0.700	1.000	< 0.001
K_{trans}	≤ 0.46	0.702 (0.584-0.804)	0.857	0.627	0.353	0.949	0.005
K_{ep}	≤ 1.14	0.926 (0.840-0.974)	0.929	0.831	0.565	0.980	< 0.001
V_e	≥ 0.4	0.849 (0.746-0.922)	0.929	0.729	0.448	0.977	< 0.001
Warthin's tumors							
ADC value	≤ 0.8	0.742 (0.626-0.837)	0.944	0.582	0.425	0.970	< 0.001
T_{peak}	≤ 19.1	0.869 (0.769-0.936)	0.667	0.909	0.706	0.893	< 0.001
WR	> 43	0.981 (0.917-0.999)	0.944	0.909	0.773	0.980	< 0.001
K_{trans}	> 0.3	0.577 (0.455-0.692)	0.889	0.346	0.308	0.905	0.291
K_{ep}	> 2.44	0.973 (0.905-0.997)	1.000	0.855	0.692	1.000	< 0.001
V_e	≤ 0.17	0.958 (0.883-0.991)	1.000	0.909	0.783	1.000	< 0.001
Malignant tumors							
ADC value	> 0.7	0.541 (0.420-0.658)	0.783	0.440	0.391	0.815	0.569
T_{peak}	≤ 120	0.531 (0.410-0.649)	0.913	0.360	0.396	0.900	0.648
WR	≤ 49	0.562 (0.441-0.678)	1.000	0.300	0.397	1.000	0.351
K_{trans}	> 0.53	0.599 (0.477-0.712)	0.652	0.600	0.429	0.789	0.194
K_{ep}	≤ 3.7	0.592 (0.471-0.706)	1.000	0.300	0.397	1.000	0.160
V_e	> 0.35	0.702 (0.584-0.804)	0.696	0.660	0.485	0.825	0.001

ADC ($\times 10^{-3}$ mm^2/s): Apparent diffusion coefficient; T_{peak} (s): Time to peak; K_{trans} (min^{-1}): Volume transfer constant between blood plasma and the extracellular extravascular space; K_{ep} (min^{-1}): Flux rate constant between the EES and plasma; V_e: EES fractional volume; AUC: Area under the ROC curve; CI: Confidence interval; PPV: Positive predictive value; NPV: Negative predictive value; WR (%): Washout ratio; EES: Extracellular extravascular space.

geneous components such as PMA have higher ADC values[1,13]. In many DWI studies involving SGTs, ADC values were reported to be useful in distinguishing BTs and MTs[6-8,17,19-21]. However, there are also studies reporting that DWI was not sufficient to make this distinction but ADC values could be useful in distinguishing some subtypes of MTs or BTs[10,22-24]. An evaluation of mean ADC values of all BTs and MTs in the present study showed that ADC values of BTs ($0.98 \times 10^{-3} \pm 0.43$ mm^2/s) and MTs ($0.95 \times 10^{-3} \pm 0.31$ mm^2/s) were similar and did not differ significantly. However, when specific tumoral subgroups were evaluated, significant differences were found in the mean ADC values among PMAs, WTs, and MTs ($P < 0.001$). In a ROC analysis using an ADC cut-off value of $> 1.1 \times 10^{-3}$ mm^2/s for PMAs, the AUC, sensitivity, and specificity were 97.7%, 100%, and 89.8%, respectively. A ROC analysis of WTs using an ADC cut-off value of $\leq 0.8 \times 10^{-3}$ mm^2/s, on the other hand, resulted in AUC, sensitivity, and specificity values of 74.2%, 94.4%, and 58.2%, respectively. These values were 54.1%, 78.3%, and 44.0%, respectively, for MTs with an ADC cut-off value of $> 0.7 \times 10^{-3}$ mm^2/s. In the present study, the mean ADC value of malignant lymphomas was $0.56 \times 10^{-3} \pm 0.05$ mm^2/s, which was well below the average ADC value of all MTs. This finding indicated that diffusion MRI could be more useful in distinguishing the subgroups within both BTs and MTs than contributing to a more general distinction between MTs and BTs.

In addition to diffusion MRI, the parameters of semiquantitative DCE MRI (TIC patterns) have also been frequently used in recent years for the differential diagnosis of SGTs[9,12,20,25,26]. On DCE MRI, TIC is obtained from signal intensity changes before the contrast agent administration, during the transition of contrast agent from the capillary bed to extravascular-intercellular distance, and during the washing of contrast agent from the tissue[1,18]. TIC patterns are correlated with tumor cellularity and vascularity[1,5,18,27]. PMAs have progressive contrast-enhancement due to low microvessel count and cellularity-stromal grade, and their washout patterns are mostly negative and, to a lesser degree, in the form of a plateau[1,27]. In the present study, type A TIC pattern (curve pattern with progression towards the late phases) was observed in all PMAs. T_{peak} values ranged from 161.80 s to 251.70 s. The

average T_{peak} value of PMAs (202.74 ± 21.48 s) was significantly longer compared to the T_{peak} values of all other SGTs. In ROC analysis of PMAs using a cut-off value of T_{peak} > 120 s, AUC, sensitivity, specificity, PPV, and NPV were 94.7%, 100%, 89.8%, 70.0%, and 100%, respectively. WTs feature rapid contrast enhancement and washout due to their high microvessel count and cellularity-stromal grade. In the present study, type B TIC pattern (T_{peak} ≤ 120 s, WR ≥ 30%) was observed in all WTs. T_{peak} values ranged from 10.80 s to 46.40 s, while WR varied from 31% to 75%. The mean T_{peak} of WTs (20.26 ± 11.72 s) was significantly shorter than that of other parotid lesions. The average WR value of WTs (59.33% ± 10.99%) was significantly higher than that of any other tumors. In ROC analysis of WTs using a cut-off value of WR > 43%, AUC, specificity, and PPV were quite high (98.1%, 94.4%, and 90.9%, respectively). Due to their high microvessel count and lower cellularity-stromal grade, MTs have rapid enhancement but their washouts tend to be slower than those of WTs[1,27]. In the present study, the mean T_{peak} value of MTs (60.60 ± 55.78 s) was significantly shorter than the T_{peak} value of PMAs. The mean WR value of MTs (18.48 ± 18.38%) was significantly lower than that of WTs, but was not different from the mean WR value of OBTs. In ROC analysis of MTs with cut-off values of T_{peak} ≤ 120 s and WR ≤ 49%, sensitivities were quite high (91.3% and 100%, respectively) but specificities were quite low (36.0% and 30.0%, respectively). A survey of semiquantitative DCE MRI studies in the literature showed that PMAs generally had type A pattern, while WTs had type B and MTs had type C TIC patterns[4,5,26]. TIC patterns are considered to have a higher diagnostic accuracy in distinguishing subgroups in SGTs compared to their power to distinguish all BTs from MTs. However, it was mentioned that TIC patterns had higher specificity especially in PMAs and WTs while their specificity in MTs was lower[4,18,25,26]. In their study with all SGTs, Lam *et al*[26] showed that all MTs except lymphomas showed type C TIC pattern (T_{peak} < 150 s and WR < 30%), while 70% of lymphomas had type B TIC pattern (T_{peak} < 150 s and WR ≥ 30%). Similar to the findings of Lam *et al*[26], 66.7% of lymphomas in the present study showed type B TIC pattern. However, unlike their findings, some other MTs showed types A, B, and D TIC patterns. There are also studies in the literature reporting that all WTs had type B TIC pattern[4,10,12]. In accordance with their findings, 100% of WTs in the present study featured type B TIC pattern. Subtypes of SGTs in the present study generally had similar TIC patterns to those reported in the literature.

The literature contains several studies on quantitative DCE perfusion MRI parameters (K_{trans}, K_{ep}, and V_e) in SGTs[3,14,15,28]. In these studies, mean K_{trans} values for PMAs ranged from 0.101 ± 0.069 min^{-1} to 0.217 ± 0.036 min^{-1}, mean K_{ep} values from 0.245 ± 0.160 min^{-1} to 0.567 ± 0.048 min^{-1}, and mean V_e values from 0.360 to 0.590 ± 0.478, while mean K_{trans} values for WTs varied between 0.105 min^{-1} ± 0.064 min^{-1} and 0.464 ± 0.036 min^{-1}, mean K_{ep} values between 0.729 ± 0.112 min^{-1} and 2.299 ± 1.312 min^{-1}, and mean V_e values between 0.1439 ± 0.093 and 0.272 ± 0.013. For MTs, mean K_{trans} values varied from 0.130± 0.035 min^{-1} to 0.327 ± 0.030 min^{-1}; mean K_{ep} values from 0.463 ± 0.103 min^{-1} to 0.784 ± 0.064 min^{-1}; and mean V_e values from 0.264 ± 0.119 to 0.445 ± 0.025. In all of these studies in the literature, the K_{trans} values of PMAs were lower than those of other SGTs[3,14,15,28]. Xu *et al*[3] found that the mean K_{trans} value of PMAs was slightly different from that of WTs (P = 0.05). Yabuuchi *et al*[14] found no significant differences among K_{trans} values of other SGTs. Huang *et al*[15] found that the K_{trans} values of PMAs were significantly lower than those of other SGTs. Similar to the results of Yabuuchi *et al*[14], in our study, mean K_{trans} value of PMAs was the lowest among all SGTs, but it was not significantly different from those of other tumors. In the studies by Xu *et al*[3], Yabuuchi *et al*[14], and Huang *et al*[15], the mean K_{ep} value was the lowest in PMAs and highest in WTs. K_{ep} values of PMAs, WTs, and MTs in the studies of both Xu *et al*[3] and Yabuuchi *et al*[14] were significantly different. However, in the study by Huang *et al* [15], the K_{ep} value of only WTs was significantly different from those of other tumors. In another study by Huang *et al*[28], significant differences were found in K_{ep} values between WTs and PMAs, and between WTs and OBTs. Similar to the results of those studies in the literature, the mean K_{ep} value in the present study was the lowest in PMAs and highest in WTs, and K_{ep} values of PMAs and WTs were significantly different from those of other tumors[3,13,14,28]. Xu *et al*[3], Yabuuchi *et al*[14], and Huang *et al*[15] found that mean V_e values of WTs were significantly lower than those of other tumors. Similar to the results of their studies, the mean V_e value of WTs in the present study was significantly lower than those of other tumors[3,14]. In another study by Huang *et al*[28], unlike other studies, the V_e value of WTs and the V_e values of PMAs and OBTs were found to be significantly lower. In ROC analysis using a cut-off value of K_{ep} ≥ 2.44 min^{-1} for WTs, the AUC, sensitivity, and specificity were 97.3%, 100%, and 85.5%, respectively. On the other hand, in ROC analysis using a cut-off value of V_e ≤ 0.17, quite high AUC, sensitivity, and specificity values (95.8%, 100%, and 90.9%, respectively) were obtained. High K_{ep} and low V_e values in WTs are explained by the limited extravascular and extracellular space in these tumors. As many studies in the literature and the present study revealed, ADC and TIC patterns of WTs could overlap with those of MTs[11]. However, similar to the findings of the studies in the literature, the present study showed that quantitative perfusion MRI parameters K_{ep} and V_e could contribute greatly to distinguishing WTs from MTs[3,14,15]. Nevertheless, our findings need to be verified by future quantitative perfusion MRI studies performed with larger series.

There are some limitations in this study. First, the parameters (number of dynamic series, acquisition time, *etc.*) varied on perfusion MRI series due to the retrospective nature of the study. Second, most of the tumors in our study were benign SGTs, and the number of MTs in the primary salivary gland was relatively low, which may have resulted in an overestimation of the diagnostic accuracy. Third, the

manual definition of ROI might have increased the variability in quantitative measurements. Although the cystic-necrotic components of the lesions were excluded from the ROI in our study, contamination of these areas can lead to significant changes in quantitative values, even if it is small in manual measurements. Fourth, for the measurements of ADC values and semiquantitative and quantitative DCE perfusion MRI parameters, interobserver agreement could not be evaluated in the study as the measurements were made by two observers with consensus.

CONCLUSION

Combined use of quantitative DCE MRI along with diffusion MRI and semiquantitative DCE MRI could help radiologists in the differential diagnosis of different subtypes of SGTs by providing higher diagnostic accuracy.

ARTICLE HIGHLIGHTS

Research background

Conventional magnetic resonance imaging (MRI) provides more data than other radiological modalities in determining the extent of tumor spread in salivary gland tumors (SGTs) and assessing its relationship to vascular and neural structures, but falls short of distinguishing subtypes of SGTs. As the malignant or benign nature of SGTs affects the treatment protocol, it is important to differentiate between malignant (MTs) and benign tumors (BTs) noninvasively with high diagnostic accuracy.

Research motivation

In recent years, advanced MRI techniques such as diffusion-weighted imaging (DWI) and semi-quantitative MRI have been increasingly used in the radiological evaluation of SGTs. However, various studies on quantitative dynamic contrast-enhanced (DCE) perfusion MRI parameters (K_{trans}, K_{ep}, and V_e) in SGTs are limited. Therefore, in this study, the effectiveness of advanced MRI applications, including all three methods, in the diagnosis of SGTs was evaluated in light of the literature.

Research objectives

To determine the diagnostic efficiency of DWI and DCE (semiquantitative perfusion) MRI and quantitative perfusion MRI parameters in SGTs.

Research methods

Apparent diffusion coefficient (ADC) values of SGTs on DWI were measured with manually inserted regions of interest, excluding the cystic components of the tumors. Time intensity curve (TIC) patterns were created for semiquantitative perfusion MRI based on T_{peak} and washout ratios (WRs) of tumors. On quantitative DCE MRI, perfusion parameters such as K_{trans} [volume transfer constant between blood plasma and extracellular extravascular space (EES)], K_{ep} (flux rate constant between the EES and plasma), and V_e (EES fractional volume) were used.

Research results

The ADC values of pleomorphic adenomas (PMAs) were significantly higher than those of Warthin's tumors (WTs), other benign tumors (OBTs), and MTs ($P < 0.001$). However, there was no significant difference in ADC values for OBTs, WTs, and MTs. PMAs had type A and WTs had type B TIC pattern while the vast majority of MTs and OBTs (54.5% and 45.5%, respectively) displayed type C TIC pattern. PMAs showed no washout, while the highest mean WR was observed in WTs. For quantitative perfusion MRI parameters, the K_{ep} value of WTs was significantly higher than those of other tumors ($P < 0.001$). For the V_e value, WTs and OBTs differed significantly from PMAs and MTs ($P < 0.001$). K_{trans} values of PMAs, WTs, OBTs, and MTs were not significantly different.

Research conclusions

DWI and semiquantitative and quantitative perfusion MRI, which provide more information on the microstructure, cellularity, interstitial distance, and vascularity of tumors, have increased the discrimination power for subtypes of SGTs.

Research perspectives

Although there is some overlap in the findings of the subtypes of SGTs obtained by advanced MRI methods, the combined use of DWI and semiquantitative and quantitative perfusion MRI will increase the power for distinguishing subtypes of SGTs.

ACKNOWLEDGEMENTS

We thank Demir O and Gürpınar AB for their help with the statistical analyses.

FOOTNOTES

Author contributions: Gökçe E designed the study; Beyhan M supervised the study; Gökçe E and Beyhan M participated in literature research and manuscript preparation, and read and approved the final version.

Institutional review board statement: This study was reviewed and approved by the Ethics Committee of the Tokat Gaziosmanpasa University Faculty of Medicine (20-KAEK-105).

Informed consent statement: Patients were not required to give informed consent for the study as figures from picture archiving and communication systems were studied retrospectively.

Conflict-of-interest statement: All the authors report no relevant conflicts of interest for this article.

Data sharing statement: No additional data are available.

Country/Territory of origin: Turkey

ORCID number: Erkan Gökçe 0000-0003-3947-2972; Murat Beyhan 0000-0002-8630-4632.

S-Editor: Liu XF
L-Editor: Wang TQ
P-Editor: Liu XF

REFERENCES

1 **Gökçe E**. Multiparametric Magnetic Resonance Imaging for the Diagnosis and Differential Diagnosis of Parotid Gland Tumors. *J Magn Reson Imaging* 2020; **52**: 11-32 [PMID: 32065489 DOI: 10.1002/jmri.27061]
2 **Lobo R**, Hawk J, Srinivasan A. A Review of Salivary Gland Malignancies: Common Histologic Types, Anatomic Considerations, and Imaging Strategies. *Neuroimaging Clin N Am* 2018; **28**: 171-182 [PMID: 29622112 DOI: 10.1016/j.nic.2018.01.011]
3 **Xu Z**, Zheng S, Pan A, Cheng X, Gao M. A multiparametric analysis based on DCE-MRI to improve the accuracy of parotid tumor discrimination. *Eur J Nucl Med Mol Imaging* 2019; **46**: 2228-2234 [PMID: 31372671 DOI: 10.1007/s00259-019-04447-9]
4 **Zheng N**, Li R, Liu W, Shao S, Jiang S. The diagnostic value of combining conventional, diffusion-weighted imaging and dynamic contrast-enhanced MRI for salivary gland tumors. *Br J Radiol* 2018; **91**: 20170707 [PMID: 29902075 DOI: 10.1259/bjr.20170707]
5 **Yabuuchi H**, Fukuya T, Tajima T, Hachitanda Y, Tomita K, Koga M. Salivary gland tumors: Diagnostic value of gadolinium-enhanced dynamic MR imaging with histopathologic correlation. *Radiology* 2003; **226**: 345-354 [PMID: 12563124 DOI: 10.1148/radiol.2262011486]
6 **Lechner Goyault J**, Riehm S, Neuville A, Gentine A, Veillon F. Interest of diffusion-weighted and gadolinium-enhanced dynamic MR sequences for the diagnosis of parotid gland tumors. *J Neuroradiol* 2011; **38**: 77-89 [PMID: 20542568 DOI: 10.1016/j.neurad.2009.10.005]
7 **Abdel Razek AA**, Samir S, Ashmalla GA. Characterization of Parotid Tumors With Dynamic Susceptibility Contrast Perfusion-Weighted Magnetic Resonance Imaging and Diffusion-Weighted MR Imaging. *J Comput Assist Tomogr* 2017; **41**: 131-136 [PMID: 27636248 DOI: 10.1097/RCT.0000000000000486]
8 **Yuan Y**, Tang W, Tao X. Parotid gland lesions: Separate and combined diagnostic value of conventional MRI, diffusion-weighted imaging and dynamic contrast-enhanced MRI. *Br J Radiol* 2016; **89**: 20150912 [PMID: 26892378 DOI: 10.1259/bjr.20150912]
9 **Mikaszewski B**, Markiet K, Smugała A, Stodulski D, Szurowska E, Stankiewicz C. Diffusion- and Perfusion-Weighted Magnetic Resonance Imaging-An Alternative to Fine Needle Biopsy or Only an Adjunct Test in Preoperative Differential Diagnostics of Malignant and Benign Parotid Tumors? *J Oral Maxillofac Surg* 2017; **75**: 2248-2253 [PMID: 28412261 DOI: 10.1016/j.joms.2017.03.018]
10 **Yabuuchi H**, Matsuo Y, Kamitani T, Setoguchi T, Okafuji T, Soeda H, Sakai S, Hatakenaka M, Nakashima T, Oda Y, Honda H. Parotid gland tumors: Can addition of diffusion-weighted MR imaging to dynamic contrast-enhanced MR imaging improve diagnostic accuracy in characterization? *Radiology* 2008; **249**: 909-916 [PMID: 18941162 DOI:

10.1148/radiol.2493072045]
11 **Gökçe E**, Beyhan M. Advanced magnetic resonance imaging findings in salivary gland tumors. *World J Radiol* 2022; **14**: 256-271 [PMID: 36160835 DOI: 10.4329/wjr.v14.i8.256]
12 **Eida S**, Sumi M, Nakamura T. Multiparametric magnetic resonance imaging for the differentiation between benign and malignant salivary gland tumors. *J Magn Reson Imaging* 2010; **31**: 673-679 [PMID: 20187211 DOI: 10.1002/jmri.22091]
13 **Munhoz L**, Ramos EADA, Im DC, Hisatomi M, Yanagi Y, Asaumi J, Arita ES. Application of diffusion-weighted magnetic resonance imaging in the diagnosis of salivary gland diseases: A systematic review. *Oral Surg Oral Med Oral Pathol Oral Radiol* 2019; **128**: 280-310 [PMID: 31029591 DOI: 10.1016/j.oooo.2019.02.020]
14 **Yabuuchi H**, Kamitani T, Sagiyama K, Yamasaki Y, Hida T, Matsuura Y, Hino T, Murayama Y, Yasumatsu R, Yamamoto H. Characterization of parotid gland tumors: Added value of permeability MR imaging to DWI and DCE-MRI. *Eur Radiol* 2020; **30**: 6402-6412 [PMID: 32613285 DOI: 10.1007/s00330-020-07004-3]
15 **Huang N**, Xiao Z, Chen Y, She D, Guo W, Yang X, Chen Q, Cao D, Chen T. Quantitative dynamic contrast-enhanced MRI and readout segmentation of long variable echo-trains diffusion-weighted imaging in differentiating parotid gland tumors. *Neuroradiology* 2021; **63**: 1709-1719 [PMID: 34241661 DOI: 10.1007/s00234-021-02758-z]
16 **Tofts PS**, Brix G, Buckley DL, Evelhoch JL, Henderson E, Knopp MV, Larsson HB, Lee TY, Mayr NA, Parker GJ, Port RE, Taylor J, Weisskoff RM. Estimating kinetic parameters from dynamic contrast-enhanced T(1)-weighted MRI of a diffusable tracer: Standardized quantities and symbols. *J Magn Reson Imaging* 1999; **10**: 223-232 [PMID: 10508281 DOI: 10.1002/(sici)1522-2586(199909)10:3<223::aid-jmri2>3.0.co;2-s]
17 **Celebi I**, Mahmutoglu AS, Ucgul A, Ulusay SM, Basak T, Basak M. Quantitative diffusion-weighted magnetic resonance imaging in the evaluation of parotid gland masses: A study with histopathological correlation. *Clin Imaging* 2013; **37**: 232-238 [PMID: 23465973 DOI: 10.1016/j.clinimag.2012.04.025]
18 **Assili S**, Fathi Kazerooni A, Aghaghazvini L, Saligheh Rad HR, Pirayesh Islamian J. Dynamic Contrast Magnetic Resonance Imaging (DCE-MRI) and Diffusion Weighted MR Imaging (DWI) for Differentiation between Benign and Malignant Salivary Gland Tumors. *J Biomed Phys Eng* 2015; **5**: 157-168 [PMID: 26688794]
19 **Milad P**, Elbegiermy M, Shokry T, Mahmoud H, Kamal I, Taha MS, Keriakos N. The added value of pretreatment DW MRI in characterization of salivary glands pathologies. *Am J Otolaryngol* 2017; **38**: 13-20 [PMID: 27806890 DOI: 10.1016/j.amjoto.2016.09.002]
20 **Tao X**, Yang G, Wang P, Wu Y, Zhu W, Shi H, Gong X, Gao W, Yu Q. The value of combining conventional, diffusion-weighted and dynamic contrast-enhanced MR imaging for the diagnosis of parotid gland tumours. *Dentomaxillofac Radiol* 2017; **46**: 20160434 [PMID: 28299943 DOI: 10.1259/dmfr.20160434]
21 **Eida S**, Sumi M, Sakihama N, Takahashi H, Nakamura T. Apparent diffusion coefficient mapping of salivary gland tumors: Prediction of the benignancy and malignancy. *AJNR Am J Neuroradiol* 2007; **28**: 116-121 [PMID: 17213436]
22 **Elmokadem AH**, Abdel Khalek AM, Abdel Wahab RM, Tharwat N, Gaballa GM, Elata MA, Amer T. Diagnostic Accuracy of Multiparametric Magnetic Resonance Imaging for Differentiation Between Parotid Neoplasms. *Can Assoc Radiol J* 2019; **70**: 264-272 [PMID: 30922790 DOI: 10.1016/j.carj.2018.10.010]
23 **Habermann CR**, Arndt C, Graessner J, Diestel L, Petersen KU, Reitmeier F, Ussmueller JO, Adam G, Jaehne M. Diffusion-weighted echo-planar MR imaging of primary parotid gland tumors: Is a prediction of different histologic subtypes possible? *AJNR Am J Neuroradiol* 2009; **30**: 591-596 [PMID: 19131405 DOI: 10.3174/ajnr.A1412]
24 **Faheem MH**, Shady S, Refaat MM. Role of magnetic resonance imaging (MRI) including diffusion weighted images (DWIs) in assessment of parotid gland masses with histopathological correlation. *Egypt J Radiol Nucl Med* 2018; **49**: 368-373 [DOI: 10.1016/j.ejrnm.2018.03.001]
25 **Ogawa T**, Kojima I, Ishii R, Sakamoto M, Murata T, Suzuki T, Kato K, Nakanome A, Ohkoshi A, Ishida E, Kakehata S, Shiga K, Katori Y. Clinical utility of dynamic-enhanced MRI in salivary gland tumors: Retrospective study and literature review. *Eur Arch Otorhinolaryngol* 2018; **275**: 1613-1621 [PMID: 29623392 DOI: 10.1007/s00405-018-4965-9]
26 **Lam PD**, Kuribayashi A, Imaizumi A, Sakamoto J, Sumi Y, Yoshino N, Kurabayashi T. Differentiating benign and malignant salivary gland tumours: Diagnostic criteria and the accuracy of dynamic contrast-enhanced MRI with high temporal resolution. *Br J Radiol* 2015; **88**: 20140685 [PMID: 25791568 DOI: 10.1259/bjr.20140685]
27 **Abdel Razek AAK**, Mukherji SK. State-of-the-Art Imaging of Salivary Gland Tumors. *Neuroimaging Clin N Am* 2018; **28**: 303-317 [PMID: 29622121 DOI: 10.1016/j.nic.2018.01.009]
28 **Huang N**, Chen Y, She D, Xing Z, Chen T, Cao D. Diffusion kurtosis imaging and dynamic contrast-enhanced MRI for the differentiation of parotid gland tumors. *Eur Radiol* 2022; **32**: 2748-2759 [PMID: 34642805 DOI: 10.1007/s00330-021-08312-y]

Published by **Baishideng Publishing Group Inc**
7041 Koll Center Parkway, Suite 160, Pleasanton, CA 94566, USA
Telephone: +1-925-3991568
E-mail: bpgoffice@wjgnet.com
Help Desk: https://www.f6publishing.com/helpdesk
https://www.wjgnet.com